



**Politecnico
di Torino**

POLITECNICO DI TORINO

Master Degree in
Nanotechnologies for ICTs

A.Y. 2020-2021

Development and characterization of an
organic field-effect based sensor (EGOFET)

Author:

Giovanna Garzone s278083

Supervisor:

Prof. Matteo Cocuzza

Co-supervisor:

Dott. Matteo Segantini

Dott. Simone Marasso

Dott. Francesca Frascella

A mia nonna

Abstract

Recently, organic electronics have increasingly gained attention for many different applications thanks to the unique properties of organic materials such as flexibility, low-cost fabrication and biocompatibility.

The latter allows organic materials to be used as active part for biosensors, mainly based on FET structure.

This work deals with the development and characterization of an Electrolyte-Gated Organic Field-Effect Transistor (EGOFET) for the detection of a tumoral biomarker known as Angiopoietin-2, using two commercially available p-type organic semiconductors (OSCs), P3HT (poly(3-hexylthiophene-2,5-diyl)) and P3CPT (poly[3-(5-carboxypentyl)thiophene-2,5-diyl]), both based on polythiophene.

The physical background is introduced in order to better understand and exploit the sensing mechanisms of the devices.

A detailed study of the stability of the two polymers under different working conditions is carried out and interesting results are obtained, suggesting the presence of some charge trapping phenomena or some electrical polarization of the OSC.

The sensing tests involving Ang-2 have provided promising results when dealing with P3CPT-based devices, for which a quite sensitive response to different concentrations of the target molecule was recorded.

Also, P3HT with the current device configuration has proven to be unable to detect Ang-2, probably due to its low capacitance with respect to the gate's one.

Contents

1	Introduction	7
1.1	Purpose of this work	7
1.2	General aspects of organic FETs and biosensors	8
2	Theoretical background	10
2.1	MOSFETs	10
2.2	Organic FETs and EGOFETs	14
2.3	Theory of EDL	16
2.4	Organic semiconductors	19
3	Materials and methods	24
3.1	Device fabrication	24
3.1.1	Chip patterning	24
3.1.2	Polymer deposition	26
3.1.3	Gate functionalization	26
3.2	Microfluidic Platform	30
3.3	Measurement set-up	32
3.4	Electrical characterization	35
3.5	Experimental protocols	39
3.5.1	Stability tests	39
3.5.2	Sensing tests	40
4	Results and discussion	42
4.1	Stability results	42
4.2	Sensing results	54
4.2.1	Device validation: BSA sensing	54
4.2.2	Angiopoietin-2 sensing	58
5	Conclusions and future works	64

List of Figures

1.1	Schematic drawing of the experimental set-up and components of EGOFET immunosensor by M. Berto et al ^[9]	9
1.2	Schematic drawing of the experimental set-up and components of EGOFET immunosensor by M. Sensi et al ^[10]	9
2.1	Simplified structure of an n-channel MOSFET ^[14]	10
2.2	Output characteristics of a MOSFET ^[14]	12
2.3	Transfer characteristic of a MOSFET. Adapted from ^[16]	13
2.4	Typical OFET device structure ^[4]	14
2.5	Simplified structure of an EGOFET ^[17]	15
2.6	Simplified electronic circuit to model an EGOFET bioelectronic sensor integrating a biorecognition layer attached to the gate ^[18]	16
2.7	Schematic representation of an EDL formation process ^[15]	16
2.8	Ethylene molecule, formation of σ and π bonds ^{[43] [44]}	20
2.9	HOMO and LUMO energy levels. The anti-bonding molecular orbital is denoted with a * ^[45]	21
2.10	Chemical structure of (a) P3HT and (b) P3CPT ^[52]	22
2.11	Lamellar configuration of P3HT (a) deposition normal to the surface (b) deposition parallel to the surface ^[56]	23
3.1	a) Silicon chip with the three interdigitated devices and contact pads, b) particular of the S/D interdigitation and the passivation window	25
3.2	Schematic representation of the lift-off process for the chip fabrication	27
3.3	Spin coating process ^[58]	27
3.4	Scheme of EDC (carbodiimide) and Sulfo-NHS crosslinking reaction ^[63]	28
3.5	Functionalized gate: on the surface of the gold a SAM of thiols is formed and a layer of specific antibodies is immobilized	29
3.6	EGOFET and microfluidic platform complete structure	30

3.7	a) PDMS microfluidics for the vertical structure b) PDMS microfluidics for the double-gate planar structure	31
3.8	(a) Probe station (b) Keysight B2912A source/meter unit	32
3.9	(a) Peristaltic pump (b) Syringe pump (c) Working principle of a peristaltic pump	33
3.10	Experimental setup in Nanoscienze Lab, DISAT	34
3.11	Output curve of a tested device	37
3.12	Transfer curve of a tested device	37
3.13	Pulsed protocol by <i>QuikIV</i> software	37
3.14	a) Transfer curve obtained with the standard measurement protocol b) Transfer curve obtained with the pulsed measurement protocol	38
3.15	Process flow of sensing measurements	41
3.16	a) EGOFET vertical structure during a stability test measurement b) EGOFET double-gate structure during a sensing test measurement	41
4.1	Effect of storage in vacuum on a) the threshold voltage V_{th} and b) the transconductance g_m for P3HT-based devices	44
4.2	Effect of storage in vacuum on a) the threshold voltage V_{th} and b) the transconductance g_m for P3CPT-based devices	45
4.3	Effect of an applied bias on a) the threshold voltage V_{th} and b) the transconductance g_m for P3HT-based devices	48
4.4	Effect of an applied bias on a) the threshold voltage V_{th} and b) the transconductance g_m for P3CPT-based devices	49
4.5	Recovery of a) the threshold voltage V_{th} and b) the transconductance g_m of P3HT after a rest period of 1 hour	52
4.6	Recovery of a) the threshold voltage V_{th} and b) the transconductance g_m of P3CPT after a rest period of 1 hour	53
4.7	Variation of a) V_{th} and b) g_m for P3HT-based devices	55
4.8	Variation of a) V_{th} and b) g_m for P3CPT-based devices	57
4.9	Variation of the maximum output current I_{max} for P3CPT-based devices	58
4.10	Preliminary Ang-2 sensing test on P3HT: the detection of the analyte cannot be proven	59
4.11	Variation of a) V_{th} and b) g_m of a P3CPT-based EGOFET during an Ang-2 sensing test. A common trend is noticeable	60
4.12	Variation of the maximum output current of a P3CPT-based EGOFET during an Ang-2 sensing test. The increasing of the current is representative of the detection of binding events	61

4.13	Variation of a) V_{th} and b) g_m of a P3CPT-based EGOFET during an Ang-2 sensing test. The detection of the binding events cannot be proven since it is not possible to recognize any particular trend	62
4.14	Variation of a) V_{th} and b) g_m of a P3CPT-based EGOFET during an Ang-2 sensing test. An opposite trend with respect to the expected one was recorded	63

Introduction

1.1 Purpose of this work

The work consists in the development and testing of an Electrolyte-Gated Organic Field-Effect Transistor (EGOFET) - based sensor by means of a deep study of its stability in time and its sensing application through electrical characterization and real-time current measurements. The purpose of the project was to find the best configuration for the sensor to be able to achieve the detection of Angiopoietin-2 (Ang-2) by playing with several parameters:

- Organic semiconductors: P3HT (poly(3-hexylthiophene-2,5-diyl)) and P3CPT (poly[3-(5-carboxypentyl) thiophene-2,5-diyl]);
- Microfluidic optimal geometry;

This research is part of the DEFLECT project, which focuses on the early diagnosis of lung cancer by means of the detection of tumor biomarkers in physiological fluids (liquid biopsy). This justifies the choice of Angiopoietin-2 as target of the sensing, being it a growth factor that plays an important role in the angiogenesis and vascular permeability related to cancer. Many studies have reported an enhanced expression of Ang-2 in lung cancer tissues ^{[1] [2] [3]}, suggesting it as a useful marker for tumor early diagnosis.

After a general overview about organic field-effect transistors (OFETs) and biosensors in chapter 1, the discussion will move to the theoretical background (chapter 2). In particular, the electrical and physical description of FETs is presented, focusing on Organic FETs and Electrolyte-Gated Organic FETs. The theory of Electrical Double Layer (EDL), on which the sensing mechanism of EGOFETs is based, is then treated followed by the detailed description of the two organic semiconductors used in this work for the realization of the sensors. Chapter 3 is dedicated to the fabrication of the sensor, the description of the measurement set-up and the measurement protocols and finally the

biological functionalization of the device. All the results about both the stability and the sensing tests are presented and discussed in chapter 4.

The whole thesis work has been carried out at Politecnico di Torino, in Nanoscience Laboratory and Chilab Materials and Microsystems Laboratory, DISAT department.

1.2 General aspects of organic FETs and biosensors

The core element of this work is a biosensor based on an Electrolyte-Gated Organic Field-Effect Transistor (EGOFET) for the detection of biological molecules.

The main idea is to have a smart and disposable sensor to be employed in clinical analysis that eventually could be exploited in point-of-care (POC) application. In this context, *electrochemical biosensors* are the ideal devices. They rely on the modification of physical/chemical characteristics of an active material due to a reaction between the bio-recognition element and the analyte. Usually they are based on a Field-Effect Transistor.

The need for a smart detection system that could be also miniaturized, scalable and low-cost drives the attention on Organic FETs instead of silicon-based ones. In fact, organic materials have several advantages: they're lighter, more flexible, they can be processed at very low temperature and with low cost technologies like printing techniques, which makes them suitable for mass production [4] [5] [6]. The possibility to have bio-compatible organic materials makes them the most promising choice for biosensors. Moreover, the functionalization of the surface with proper biological receptors allows for high selectivity, that is one of the most important features a biosensor is required to have [6].

The device of interest of this work, the EGOFET, is a further evolution of OFETs, where an electrolyte is included in the structure. Its presence is a crucial element for biological applications since it allows operation in aqueous environments, so that even the use of water as liquid electrolyte was reported [7]. Moreover, EGOFETs display much higher gate capacitance (up to ~ 1000 higher) than other types of OFETs and this allows to work at much smaller voltages than those necessary for OFETs ($< 1 V$ instead of $> 10 V$ or even higher) [8].

All these features, in addition to the ones previously discussed about the organic material, make EGOFETs the most promising candidate for the development of new

biosensors.

In recent years, examples of EGOFET-based biosensors can be easily found for the detection of pro-inflammatory cytokines ^[9] ([fig. 1.1]), drugs^[10] ([fig. 1.2]), enzymes ^[11], dopamine ^[12] and a lot of other applications, justifying the high interest these devices have acquired as part of a new frontier of biosensing.

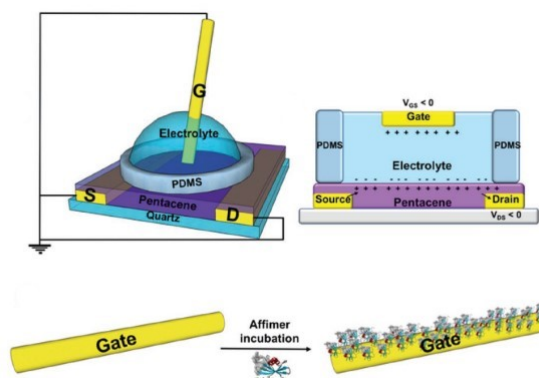


Figure 1.1: Schematic drawing of the experimental set-up and components of EGOFET immunosensor by M. Berto et al ^[9]

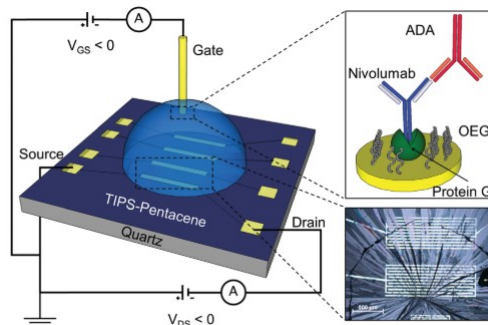


Figure 1.2: Schematic drawing of the experimental set-up and components of EGOFET immunosensor by M. Sensi et al ^[10]

Theoretical background

As already said, EGOFETs belong to the family of OFETs, from which they differ for the presence of an electrolyte replacing the gate oxide. In this case, the electrolyte is liquid and it electrically couples the organic semiconductor with the gold gate.

When a voltage is applied to the gate, the ions in the electrolyte will rearrange on the gate/electrolyte and polymer/electrolyte interfaces depending on their charge sign, so two EDLs are formed. For this reason it is also convenient to introduce the physical aspects of EDL to fully understand the working principle of the device, along with a discussion about the organic semiconductors used in this work.

Unfortunately, a definitive model for the OFET transport mechanism is still to be developed. Anyway, the MOSFET model can be applied in a first approximation to electrically describe the device behavior [4] [13].

2.1 MOSFETs

A simplified structure of an n-channel MOS is shown in [fig. 2.1]. It is composed by a p-doped silicon substrate called *body*, an oxide layer covering the center part of the body, an electrode called *gate* on the top of the oxide and two lateral heavily n doped regions (opposite to the body doping type) called *source* and *drain*. The region between source

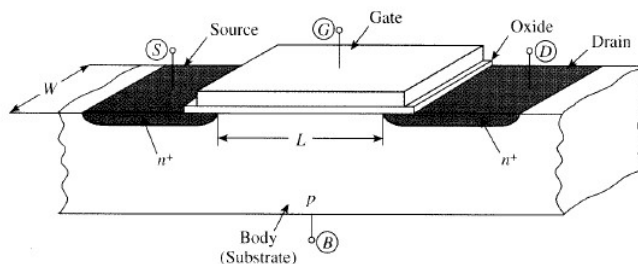


Figure 2.1: Simplified structure of an n-channel MOSFET [14]

and drain, where current flows, is called *channel*.

For an n-channel MOS as in [fig.2.1], a positive voltage applied on the gate electrode V_{GS} can attract the electrons from the n^+ regions below the oxide, where they will fill the holes due to the p-doping of the body and they will form the *n-channel*. In case of reverse doping type, a negative V_{GS} is required to have a holes current flow and the MOS is said to be a *p-channel* MOS.

It is important to remember that MOSFETs are threshold-based devices, that is $|V_{GS}|$ has to be bigger than a threshold value V_{th} in order to switch on the device.

Depending on V_{GS} , three operational modes are possible. For the n-MOS [4] [14] [15] these are:

- **Accumulation regime:** when $|V_{GS}| \ll V_{th}$ an electric field from the substrate towards the gate is created. This means that the gate electrode is negatively charged so positive charges, i.e. holes, accumulate at the surface of the substrate for charge balance;
- **Depletion regime:** As V_{GS} increases and overcomes the so called *flat band potential* V_{FB} (voltage value at which the energy bands of the system are flat), the gate becomes positively charged. The holes in the substrate are repelled so the surface is depleted of charges;
- **Inversion regime:** V_{GS} is sufficiently high to attract electrons from the source to the surface, so that an inversion layer is formed and the conductive channel connects the source and the drain.

The current flowing in the device I_{DS} is measured as function of the voltage applied between source and drain V_{DS} , that is responsible for the actual movement of charges, provided that $|V_{GS}| > V_{th}$. The typical behavior of $I_{DS}(V_{DS})$ is shown in [fig. 2.2], where three regions can be easily noticed [16].

- For small V_{DS} , the channel behaves as a linear resistance and the value of the current is simply given by

$$I_{DS} = \frac{\mu C_{ox} W}{L} [(V_{GS} - V_{th})V_{DS}] \quad (2.1)$$

This is called **linear region**;

- At higher V_{DS} , the voltage drop across the channel increases gradually from the source towards the drain and consequently the voltage between the gate and the

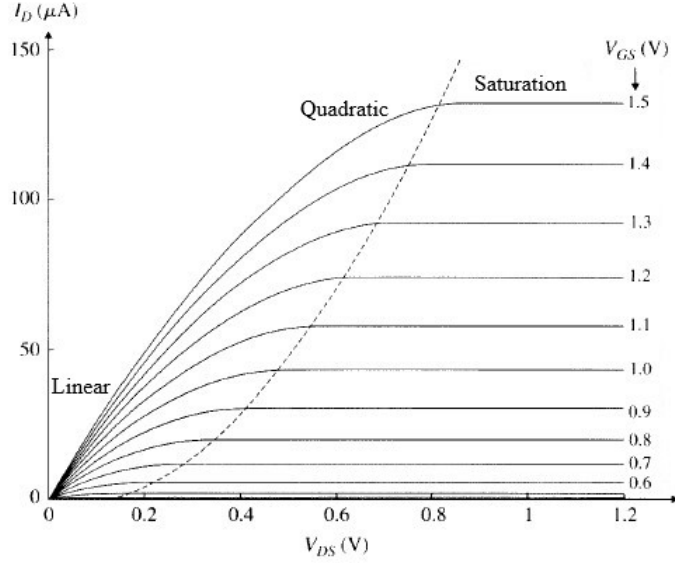


Figure 2.2: Output characteristics of a MOSFET [14]

channel decreases from the source to the drain. Since the channel depth depends on this voltage, it is no more uniform and its resistance increases. Hence the behavior of the current is not linear anymore but it is given by a quadratic expression, leading to the **quadratic region**:

$$I_{DS} = \frac{\mu C_{ox} W}{L} \left[(V_{GS} - V_{th})V_{DS} - \frac{1}{2}V_{DS}^2 \right] \quad (2.2)$$

- When $V_{DS} > (V_{GS} - V_{th})$ the device is said to be in **saturation region** since every further increase of the voltage does not affect the current anymore. This happens because the channel at the drain has reached zero depth (so called *pinch-off*), so the current saturates at:

$$I_{DS} = \frac{\mu C_{ox} W}{L} V_{DS,sat}^2 \quad (2.3)$$

where $V_{DS,sat} = (V_{GS} - V_{th})$

In these equations, W is the width of the channel, L is the length, μ is the mobility of the carriers responsible for the current flow and C_{ox} is the oxide capacitance per unit gate area. Typically, C_{ox} is in the order of femtoFarad ($fF = 10^{-15} F$), L is in the range of $[0.03 - 1] \mu m$ and W is in the range of $[0.05 - 100] \mu m$ [16].

Another important electrical characteristic to consider is the *transfer characteristic*, namely the behavior of the current I_{DS} depending on the gate voltage V_{GS} when the drain-source voltage is fixed in the saturation regime ([fig. 2.3]).

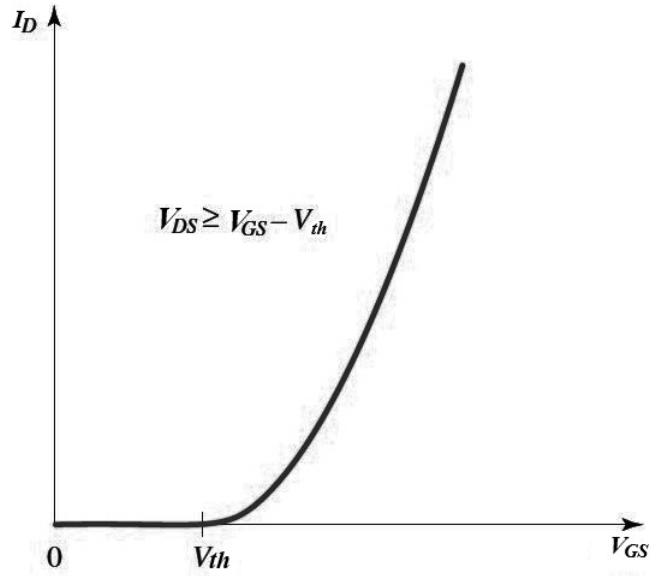


Figure 2.3: Transfer characteristic of a MOSFET. Adapted from ^[16]

In this region, I_{DS} goes quadratically with V_{GS} , being $V_{DS} = V_{GS} - V_{th}$. It is easy then to extract one of the most important figure of merit of the device, the *threshold voltage* V_{th} , that gives information about the switching of the MOS, through the intersection of $\sqrt{I_{DS}}$ and the horizontal axis V_{GS} .

One could also calculate the *transconductance* g_m , that tells how much the channel current is sensible to variations of the voltage V_{GS} . Graphically, it is the slope of the transfer curve and it can be derived from eq. 2.3 as

$$g_m = \frac{\partial I_{DS}}{\partial V_{GS}} = \mu C_{ox} \frac{W}{L} (V_{GS} - V_{th}) \quad (2.4)$$

2.2 Organic FETs and EGOFETs

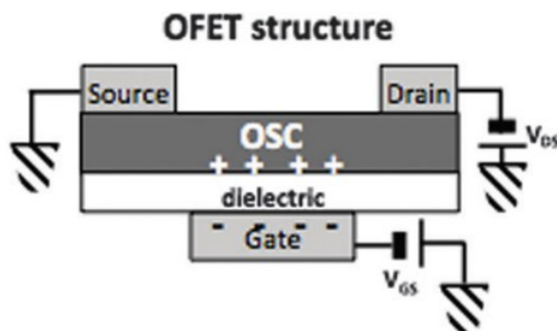


Figure 2.4: Typical OFET device structure ^[4]

OFETs are a modification of the previously discussed MOSFET. A typical OFET consists of an organic semiconductor film, three electrodes (gate, source, and drain), and a gate dielectric (insulator) ([fig. 2.4]).

Its working principle is basically the same of the MOSFET, except for the working regime. Considering a p-type organic semiconductor, the application of a negative V_{GS} leads to the formation of an *accumulation layer* of positive charges at the organic semiconductor (OSC)/insulator interface, so the device is said to operate in *accumulation mode*.

The transport mechanism is different too: while for inorganic semiconductors charges move through the channel thanks to drift through a band of states, in organic materials carriers move by sequential *hopping* between different states. Because of this, the conducting channel is highly sensitive to external stimulus, so that OFETs can be utilized as sensors ^[5]

A detailed description of organic semiconductors and their electrical properties will be addressed in the following chapter.

EGOFETs are a further modification of OFETs: the gate electrode is separated from the organic semiconductor by an electrolyte and source and drain electrodes, isolated from the electrolyte, provide electrical contact to the channel [fig. 2.5].

Only capacitive processes occur for EGOFETs ^[8]. In fact, considering a p-type EGOFET with a negative V_{GS} applied on the gate, positive ions will accumulate at the gate/electrolyte interface and negative ions will accumulate at electrolyte/semicon-

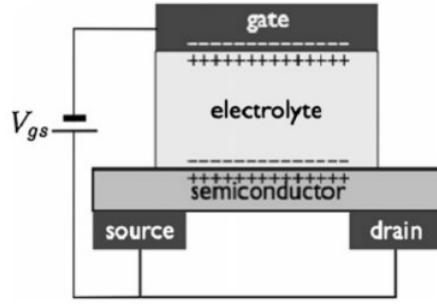


Figure 2.5: Simplified structure of an EGOFET ^[17]

ductor interface. This in turn leads to accumulation of positive charges (i.e. holes) in the topmost layer of the organic semiconductor, that is the formation of *Electrical Double Layer (EDL)*, making the channel conductive and allowing the flow of current.

The aqueous environment allows the possibility to guarantee bio-compatibility and in-situ sensing of molecules. Moreover, the functionalization of a surface in contact with the electrolyte provides very high selectivity to the sensor. Both gate and OSC surface can be modified with different techniques, even though gate functionalization is to prefer since it is normally isolated from the channel regions, thus channel properties are not affected ^[6].

The EDL can be seen as a capacitor whose capacitance is inversely proportional to the charge separation. Its thickness is extremely small, typically less than 0.1\AA in metals and few \AA in electrolytes, so the capacitance can reach tens of $\mu\text{F}/\text{cm}^2$, which enables the transistor to be operated at very low potentials ^[17].

Some attempts to derive a specific model for EGOFETs were recently done by Tu D. et al. ^[19] ^[13], who proposed a dc model to simulate the static performance of EGOFETs. Basically, the charges accumulated in the channel are considered being contributed from voltage-dependent EDL capacitance and the voltage-dependent contact effect and short-channel effect are also taken into account with the introduction of two parameters χ and γ , *EDLC voltage-dependent factor* and *Enhancement Mobility factor* respectively.

Anyway, MOSFET equations turn out to be well suited and predictive for the electrical description of these devices, so that all the derivation of the most important figures of merit when dealing with the sensing experiments in this work will follow the methodology previously discussed.

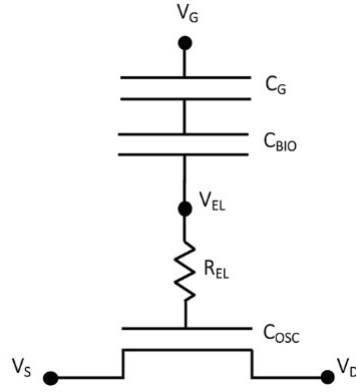


Figure 2.6: Simplified electronic circuit to model an EGOFET bioelectronic sensor integrating a biorecognition layer attached to the gate [18]

2.3 Theory of EDL

An Electric Double Layer (EDL) is formed when an electric field is applied between two electrodes separated by an electrolyte (liquid or solid). More specifically, when a voltage is applied, cations and anions composing the electrolyte are attracted towards the surface of the electrode that is oppositely polarized in order to satisfy the charge balance. Thus the EDL is the space including the charge layer of the electrode surface and the ions of the electrolyte, as shown in [fig. 2.7].

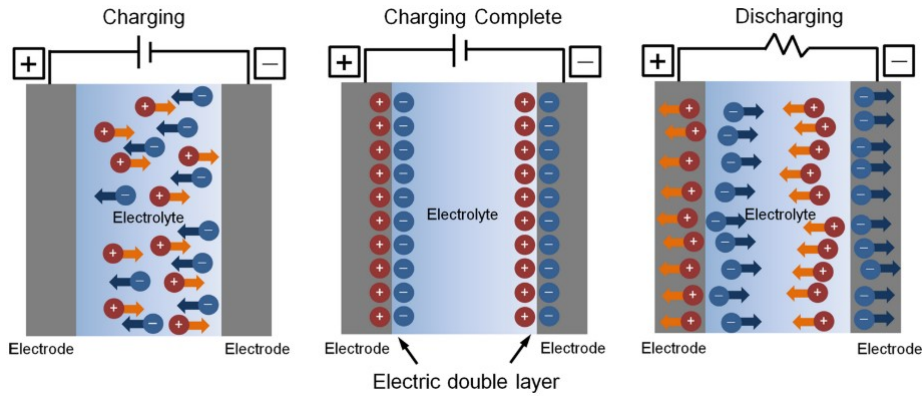


Figure 2.7: Schematic representation of an EDL formation process [15]

More accurately, the charge layer in the electrolyte is further composed by two layers: the *Stern layer* and the *diffuse layer* [20]. The former is the very first layer of ions that are strongly absorbed on the electrode surface due to the high electrostatic attractive force, while the latter is composed of mobile charges of the electrolyte that move thanks to the

electrostatic interaction. Rigorously, also the Stern layer can be divided in two further layers, *Inner Helmholtz Layer* and *Outer Helmholtz Layer*, depending on whether the ions are specifically or non-specifically adsorbed. Of course, the excess of ions decreases with the distance from the electrodes and the dimension of the diffuse layer decreases with increasing ions concentration.

The EDLs at the interfaces can be considered as nanometer-thick capacitors. The capacitance estimation is generally assumed to follow that of a parallel-plate capacitor [20]:

$$C = \frac{\epsilon_r \epsilon_0 A}{\lambda}$$

where ϵ_0 is the vacuum permittivity, ϵ_r is the effective dielectric constant of the EDL, and λ is the *Debye screening length*, that is the thickness of the double layer.

More specifically, the total capacitance of the EDL is given by the series of the Stern layer's and the diffuse layer's capacitances:

$$\frac{1}{C_{tot}} = \frac{1}{C_{Stern}} + \frac{1}{C_{diff}} \quad (2.5)$$

and it is governed by the smaller of the two, typically C_{Stern} .

It is easy to demonstrate that thanks to the formation of the Stern layer within only a few Å, very large capacitances are achieved. In fact, considering a typical value of $\lambda \sim 1 \text{ nm}$, $C_{tot} > 1 \mu\text{F}/\text{cm}^2$ can be reached, which exceeds the capacitances of conventional 'high- k ' dielectrics such as Ta_2O_5 by an order of magnitude [21].

The Debye length is the characteristic distance over which the electric field is screened by the charges of the EDL and it defines the exponential decay of the potential in the electrolyte:

$$\varphi(z) = \zeta \exp\frac{-z}{\lambda} \quad (2.6)$$

where ζ is the so called *zeta potential*, that is the potential at the beginning of the EDL ($\varphi(z = 0)$).

Rigorously, the exponential decay occurs in the diffuse layer only, while the Stern layer is concerned with a linear drop of the potential, so the zeta potential should be defined as $\varphi(z = z_{diff})$ at the beginning of the diffuse layer.

The Debye length is specific of each solution and it is defined by:

$$\lambda = \sqrt{\frac{D\epsilon}{\sigma}}$$

where D is the Diffusion constant of the electrolyte, ϵ is the dielectric constant and σ is the ionic charge of the electrolyte.

In sensing application, λ is an important parameter to consider since it represents the distance over which detection is not possible anymore ^[22], even though more recent researches have proven that detection beyond Debye length is possible ^{[23] [24]}.

For instance, Palazzo et al. ^[23] demonstrated an EGOFET sensor capable to detect events at distances that are 30 times λ also in presence of high salt concentrations. The mechanism of sensing was ascribed to an additional in-series capacitance due to the protein layer of the gate functionalization that was shown to be insensitive to the Debye length value.

Anyway, generally a trade-off is necessary: it would be desirable to have large EDLs in order to increase λ through diluted solutions, but biological applications require highly concentrated solutions. For example, as will be discussed later, in this project PBS 0.01x with $\lambda = 7.3 \text{ nm}$ ^[22] was exploited to work with anti-Ang-2 antibodies (typically, antibodies size is around $\sim 5 - 15 \text{ nm}$ ^[25]).

It is easy to understand that the sensing process is possible thanks to the properties of EDL: when a reaction occurs between the biochemical receptor and the target, the interfacial potential changes and it leads to the channel current response by the EDL capacitive effect ^[26].

Moreover, it has been proven that the charge injection from the source electrode ^[27] and the threshold voltage of the device ^[28] are highly influenced by the gate work function, that is specific of each metal. Therefore it is reasonable to assume that the effective gate potential is affected by the binding events that modify the capacitance of the bilayer C_{BIO} ([fig. 2.6]) and consequently a variation in the threshold voltage and/or the drain current of the device can be observed ^[18].

2.4 Organic semiconductors

Recently, organic materials have been extensively employed in large-area electronics, such as displays [29] [30], wearable electronics [31] [32] [33], solar cells [34] [35] [36], and much more complex applications thanks to their unique properties as light weight, mechanical flexibility, availability, affordability, and easy low-cost processing techniques such as printing, dip-coating, drop casting, grafting and more "exotic" techniques like nano-imprinting technologies [37] [38] [39].

Differently from inorganic materials, organic compounds have a *disordered* structure [40], i.e. they do not present a perfect long-range crystalline structure. Consequently they do not have a properly defined band structure and energy bands and charges are localized on single molecules with the charge transport limited by the so-called *hopping* mechanism [41].

In organic compounds, carbon atoms undergo hybridization of their orbitals. It consists in a *linear combination* of the s and type atomic orbitals during the bonding of atoms, so that new molecular orbitals are formed. Depending on the number of p orbitals involved in this process, there can be three different types of hybridization:

- **sp** hybridization, when the valence s orbital mixes with one of the valence p orbitals leading to the formation of two new equivalent hybrid orbitals in a planar geometry;
- **sp²** hybridization, when the valence s orbital mixes with two valence p orbitals leading to the formation of three new equivalent hybrid orbitals;
- **sp³** hybridization, when the valence s orbital mixes with all the three p valence orbitals leading to the formation of four new equivalent hybrid orbitals in a tetrahedral geometry.

Considering the ethylene molecule, where C atoms are hybridized sp², the overlapping of the hybridized orbitals gives rise to the so-called σ bond, while the remaining p orbitals establish the so-called π bond perpendicularly. The electron cloud is delocalized between the two atoms ([fig. 2.8]) and the electrons can move from one carbon atom to another; such a delocalized structure is characterized by "conjugation" [42]. All the organic macromolecules that are characterized by a backbone of alternating single and double bonds (so that the overlapping of p-orbitals creates a system of delocalized electrons) are said to be " π -conjugated systems".

When the wave functions describing the orbitals are in-phase and their combination is characterized by a constructive interference, the final molecular orbital is a low-energy one and it is said to be *bonding*, otherwise the high-energy *anti-bonding* orbital is formed. Therefore the molecule's energy levels are divided into *HOMO* (Highest Occupied Molecular Orbital) and *LUMO* (Lowest Unoccupied Molecular Orbital), with a gap in between, as represented in [fig. 2.9]. For Organic Semiconductors (OSCs), since the energy splitting of π bonds is smaller than that of σ bonds, electronic processes occur energetically favorably on p orbitals [42].

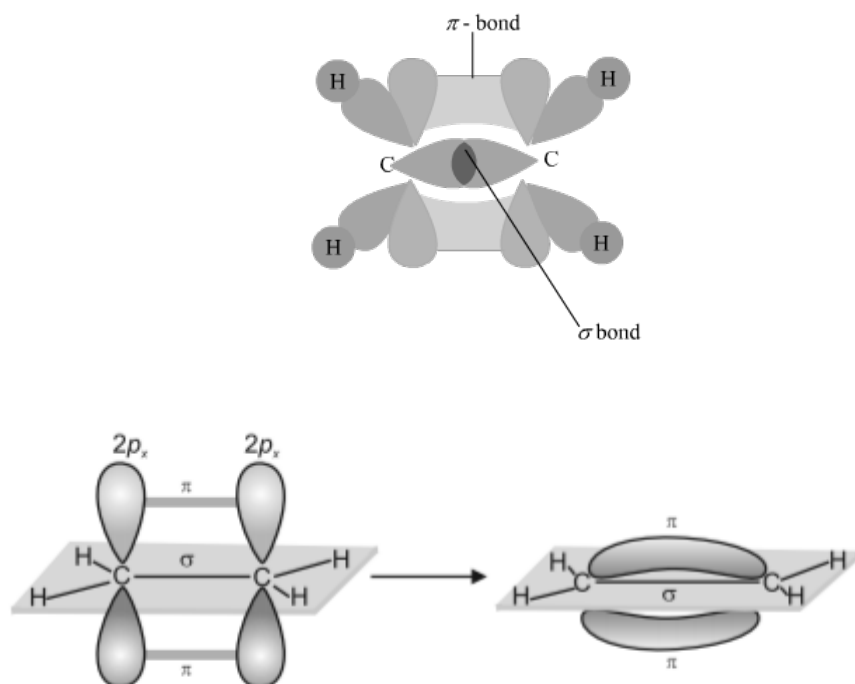


Figure 2.8: Ethylene molecule, formation of σ and π bonds [43] [44]

As already mentioned, the lack of a defined band structure is reflected in a particular type of carrier transport: the *hopping*. Differently from crystals, that are characterized by drift transport in conduction or valence band (depending on the charge carrier), in OSC the conjugated states are separated by energy and space so a continuous transport of carrier is not possible. Hopping can be seen as a thermally activated tunnel effect of electrons between conjugation units [41]. The transition probability between two states is therefore based on phonon-assisted tunnel effect and it is described by the Miller-

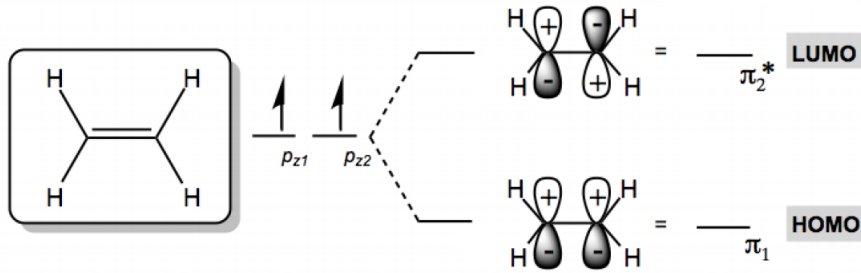


Figure 2.9: HOMO and LUMO energy levels. The anti-bonding molecular orbital is denoted with a π_2^* [45]

Abrahams model, which combines an Arrhenius dependence on the temperature and an exponential dependence on the distance between the two levels involved in the jump [46].

Later, the model was refined by Rudolf A. Marcus (Nobel prize, 1992). In his model, the transition of an electron between two states is no more a simple tunneling problem, but it can be seen as an exchange of a polaron (that is a quasi-particle representing the combination of the charge and the lattice distortion [40]), so that also the polaron binding energy plays an important role in the transport rate [47].

Given the hopping-based nature of the charge transport mechanism, the mobility associated to the OSC - based transistors is much smaller compared to the one of inorganic FET [48].

In order to achieve high carrier mobilities, it has been shown that high long-range order of the polymer chains is an important factor. In this way, efficient chain interconnections between the sites of the polymer are assured [49].

Crystalline polymers turn out to be the best candidates for high-mobility applications. In this work, P3HT (poly(3-hexylthiophene-2,5-diyl)) and P3CPT (poly[3-(5-carboxypentyl) thiophene-2,5-diyl]) have been used and their chemical structure is reported in [fig. 2.10]. They are both composed by a polythiophene backbone and only differ on the terminal group on their side chain. In fact, P3CPT has a terminal carboxyl group (-COOH) in the side chain, while P3HT has a methyl group (-CH₃). The side chains also are responsible for the solubility of the two polymers in several solvents (for example chloroform), since polythiophenes are generally insoluble [50].

In this regard, when dealing with the processing of the OSC to get the thin film of the EGO-FET structure, the choice of the solvent is crucial for the final quality of the film, besides improving the solubility of the polymer. For example, it was demonstrated that oDCB (orthodichlorobenzene) for P3HT has an important role in enhancing the polymer crystallization so that a high-quality film is obtained. ^[51]

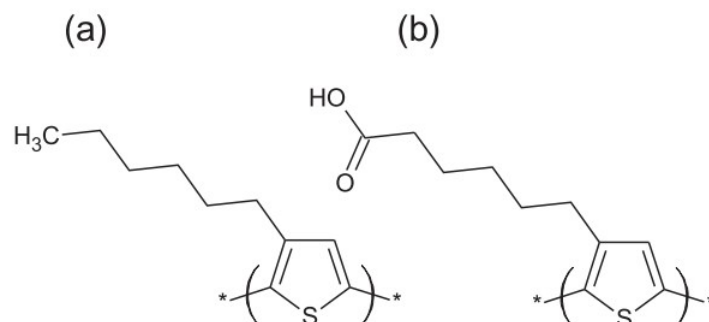


Figure 2.10: Chemical structure of (a) P3HT and (b) P3CPT ^[52]

The high value of mobility is due to the morphology of the polymer films: in fact, it was demonstrated that P3HT self-organizes in a lamellar structure with two-dimensional conjugated sheets formed by inter-chain stacking ^[48] ^[18].

Of course, the alignment of polymer backbones results in a mobility anisotropy that is an important parameter to consider in a device-design context. It was proven that the lamellar configuration normal to the deposition surface provides mobility values that are 100 times higher than horizontal configuration ^[48] [fig. 2.11].

The alkyl chain provides P3HT an hydrophobic behavior, confirmed by the contact angle of about 105 °, while a smaller value was found for P3CPT (49 °) ^[53]. This leads to huge behavior differences: P3CPT is much more susceptible to ion penetration, leading to electrochemical doping that can affect both surface and bulk of the OSC, even if several studies demonstrated that charges are stored mostly inside the bulk ^[52].

Concerning P3HT, if on the one hand the strong hydrophobic behavior could lead to some challenges in the polymer deposition ^[53], on the other it could be beneficial for stability: it was demonstrated that direct contact with water reduces the effect of degradation of the polymer if compared to exposition to air ^[54].

By contrast, the better wettability of P3CPT simplifies the manufacturing challenges but can affect its stability in time ^[53].

The terminal groups, and primarily the carboxyl group of P3CPT, can be directly exploited to immobilize biomolecules, making possible to work in a biosensing framework [55]. As already said, since the sensing principle is based on a capacitive effect, the differences in the capacitance values of the polymers are to be considered and can be crucial in the sensing application. Specifically, P3HT is characterized by a much lower capacitance $C_{OSC} = 3 \mu F/cm^2$ with respect to that of P3CPT that is $C_{OSC} = 40 \mu F/cm^2$ [52].

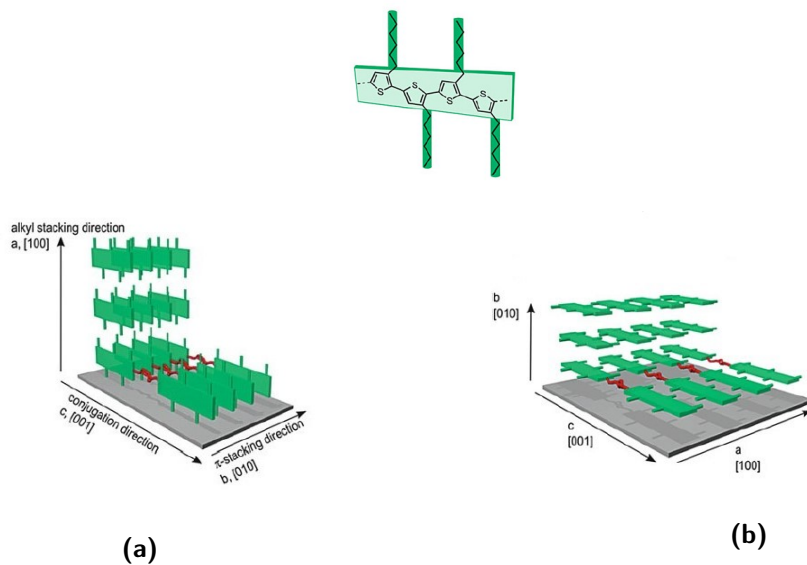


Figure 2.11: Lamellar configuration of P3HT (a) deposition normal to the surface (b) deposition parallel to the surface [56]

Materials and methods

The device is overall composed of four elements:

- PMMA holders to support all the elements of the device;
- Two complementary patterned PDMS layers forming the microfluidics;
- Chip with three parallel inter-digitated devices, over which the polymer is deposited;
- Gold gate electrode;

In this chapter, the fabrication of each element is presented, along with the description of the measurement setup and all the electrical characterizations.

All the processes are carried out at Chilab - Materials and Microsystems Laboratory (DISAT, Politecnico di Torino), unless differently specified.

3.1 Device fabrication

3.1.1 Chip patterning

Each chip hosts three independent interdigitated electrodes, with the corresponding contact pads [fig. 3.1].

The devices are obtained starting from a 4-inch p-type $\langle 100 \rangle$ silicon wafer terminated with a $1\ \mu\text{m}$ thick thermally-grown oxide layer.

The electrodes are fabricated through a lift-off process, schematically represented in [fig. 3.2].

An adhesion promoter (Ti prime) was spin-coated at 4000 rpm for 30s and then baked at 120°C for 2 minutes. This step ensures the adhesion of the photoresist, which is fundamental for patterning features in the range of tens of micrometers. The AZ 5214 E

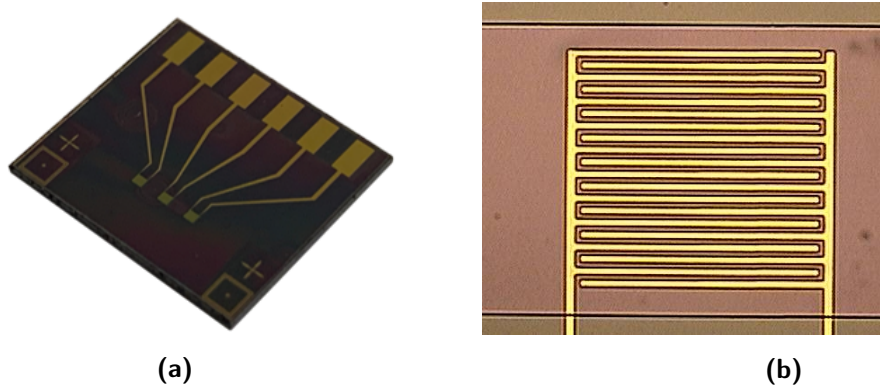


Figure 3.1: a) Silicon chip with the three interdigitated devices and contact pads, b) particular of the S/D interdigitation and the passivation window

was then spin-coated at 4000 rpm for 30 seconds and then baked at 105°C for 2 minutes. The pattern is transferred on the wafer thanks to the exposure to UV light with a mask (previously fabricated with the laser writer Microtech LW-405) for 6.5 seconds, followed by a reversal bake of 2 minutes at 105°C. Finally, a flood exposure (i.e. without mask, exposing the whole wafer) to UV light is performed for 21.5 seconds. The wafer is then rinsed in AZ 726 MIF developer for 30 seconds to remove the unwanted photoresist.

Compared to standard resists, the image reversal photoresist requires two additional steps: the *reversal bake* and the *flood exposure* process, which make the first exposed areas insoluble in the developer and then the un-exposed areas able to be developed [57].

After that, a Ti adhesion layer (10 nm) followed by an Au layer (100 nm) are deposited onto the wafer with an e-beam evaporator (ULVAC EBX- 14D). The lift-off process is then finalized by stripping the photoresist with acetone for around 30 minutes. The length of the obtained channel is 10 μm and the width is 9.96 μm .

A 150 nm passivation layer of Al_2O_3 is deposited with e-beam evaporation and then patterned again with the same lift-off process previously described in order to expose the active channel area and the contact pads.

A protective layer is then deposited on the whole wafer and the dicing of the chips is performed through laser cutting technology (Microla Optoelectronics Srl), obtaining 36 chips of 12.8mm x 11.8 mm.

3.1.2 Polymer deposition

After a preliminary cleaning step to remove the protective layer through acetone and isopropyl alcohol, the two organic semiconductors, both purchased from Rieke Metals, are deposited on each chip by spin coating (illustrated in [fig. 3.3])^[58], with the SPIN 150i spin coater.

The deposition process is the same for the two polymers. The only difference is the employed solvent, which is orthodichlorobenzene (oDCB) for P3HT and Dimethyl sulfoxide (DMSO) for P3CPT. Here are the steps followed for the deposition:

- Preparation of the OSC solution: P3HT (P3CPT) is dissolved in oDCB (DMSO) to get a 2.5 mg/ml concentrated solution, that is heated on a magnetic stirrer to achieve homogeneity;
- Spin coating: 50 μ l of solution are deposited on the chip (previously heated at 110 °C for 10 minutes to remove any water trace after its cleansing) with a micro-pipette and then spin coated for 5 seconds at 500 rpm and for 30 seconds at 2000 rpm. Two deposition steps are performed to improve the homogeneity of the film;
- Baking: the chips are baked at 75 °C for 2 hours in vacuum.

3.1.3 Gate functionalization

The functionalization process was performed at the Nanoscienze LAB in Politecnico di Torino, exploiting rectangular wafer chips (11.8 mm x 7.8 mm) covered with 100 nm of e-beam evaporated Au.

The core concept of this work is to detect the presence of Ang-2 in a fluid through a variation of the output signal of the device that occurs only if Ang-2 binds with its specific antibody tethered on the gold gate. This means that the gate has to be properly functionalized with a strong strategy that allows the immobilization of reagents on the surface. The method used in this work involves the formation of a Self-Assembly Monolayer (SAM)^[59] of thiols on gold surfaces that will serve as anchoring point for the antibodies layer^[60] and it is usually exploited to arrange organic layers on inorganic substrates^{[61] [62]}.

Each gold gate is cleaned with acetone and isopropyl alcohol, then it is immersed in a 10 nM 3-MercaptoPropionic Acid (MPA) solution (composed of 5 ml of ethanol and 4.4 μ l

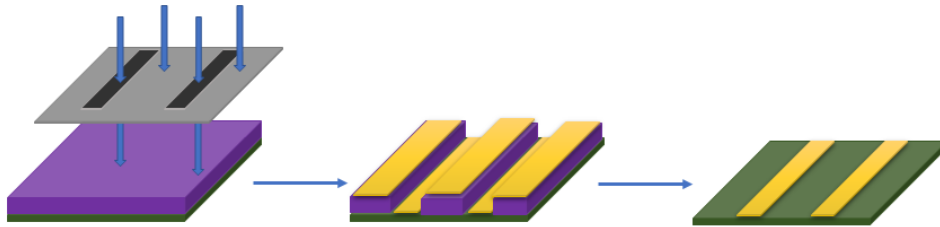


Figure 3.2: Schematic representation of the lift-off process for the chip fabrication

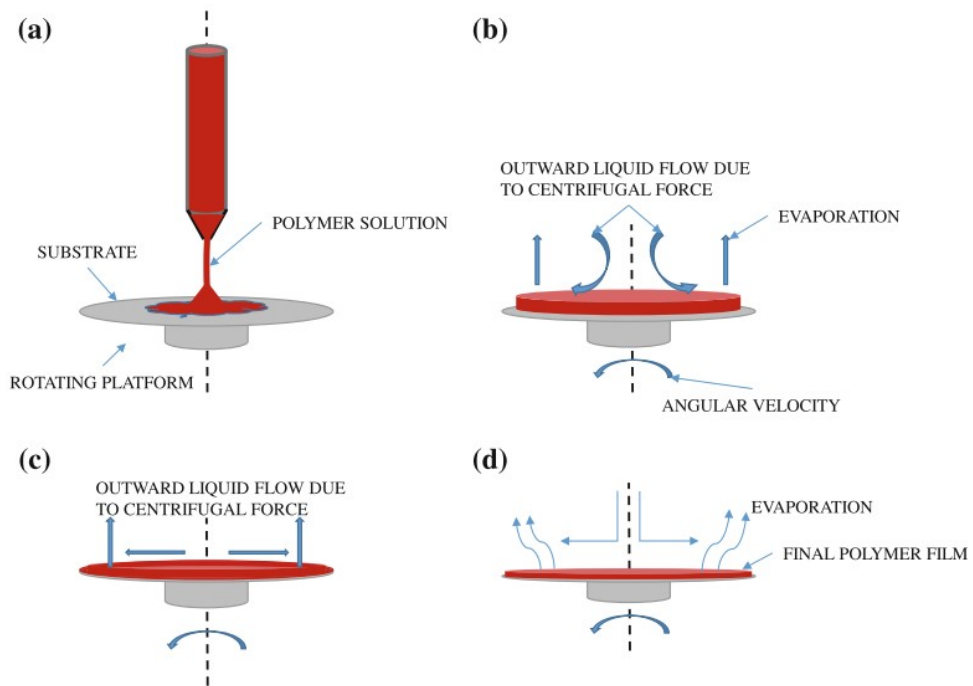


Figure 3.3: Spin coating process [58]

of MPA) and left 1 hour in incubation at room temperature to allow the formation of the SAM. Then, two subsequent immersion in ethanol and one in distilled water (Ultrapure Water grade) are performed to clean the samples.

After drying with nitrogen, the gates are placed in a 24-multiwell plate with 500 μl of 50 nM 2-(N-morpholino)ethanesulfonic acid (MES) buffer for 15 minutes.

A solution of 2 ml MES, containing 4 mM 1-Ethyl-3-(3-dimethylaminopropyl)-carbodiimide hydrochloride (EDC, 1.5 mg) and 10 mM N-hydroxy-sulfosuccinimide sodium salt (sulfo-NHS, 4.3 mg) is prepared. Each gate is immersed in 500 μl of this solution for 15 minutes, then three steps of PBS washing of 5 minutes each are performed.

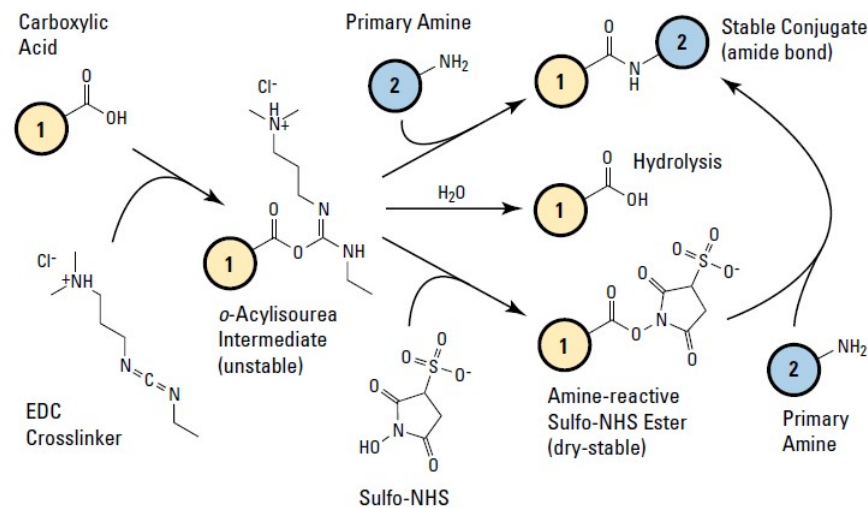


Figure 3.4: Scheme of EDC (carbodiimide) and Sulfo-NHS crosslinking reaction [63]

All these steps are required to increase the reactivity of -COOH terminal groups exposed by the thiols towards primary amines, so that a strong amide bond is formed with the biorecognition element and eventually the layer of antibodies needed for the biosensing activity is immobilized on the surface [fig. 3.4]. This technique is called *amide coupling* [63] [64].

At this point, the layer of antibodies can be deposited on the surface. Each gate is covered by 80 μl of a solution containing 5 $\mu\text{g}/\text{mL}$ of anti-Ang-2 specific antibody (500 μl of PBS and 0.5 μl of a 0.5 mg/mL antibodies stock solution) and then incubated overnight at 4 °C.

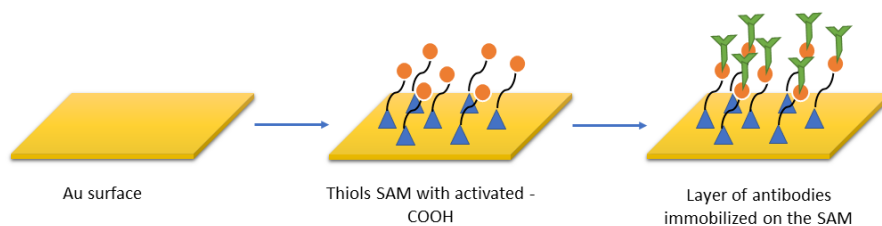


Figure 3.5: Functionalized gate: on the surface of the gold a SAM of thiols is formed and a layer of specific antibodies is immobilized

After the incubation, three washing steps of 5 minutes each with 500 μl of PBS enriched with 0.05% tween (v/v) are performed for each gate in order to clean the samples and to get rid of any un-bond material.

In [fig. 3.5], the final appearance of the functionalized gate is depicted, showing the binding sites available for the target to be detected.

Two types of sensing tests were performed: one for the biosensor validation and one for the effective sensing of Ang-2, therefore the former involved the functionalization of the gates with anti-BSA to detect BSA while the latter with anti-Ang-2 to detect the tumoral biomarker.

3.2 Microfluidic Platform

The microfluidic platform is designed to host and guide the fluids over the device, allowing a continuous flow of the several solutions to be tested.

It consists of PDMS-made fluidic chamber and two holders made of PMMA that guarantee the sealing of the whole structure and the integration of the chip and the gate electrode, as seen in [fig. 3.6].



Figure 3.6: EGO-FET and microfluidic platform complete structure

The channels are fabricated through replica molding techniques: the PDMS is fabricated by mixing *Sylgard 184* silicone elastomer and the curing agent in a 10:1 weight mixing ratio and then casted into the master, after a vacuum treatment to get rid of air bubbles. The master was obtained by PolyJet[®] 3D-printing (Objet30 by Stratasys) using *VeroWhite* resin, a liquid photosensitive polymer that polymerizes layer by layer under UV light exposure. An additional overnight annealing and a subsequent sonication in acetone is required in order to make masters suitable for the molding process. The pieces are then baked at 90 °C and carefully extracted.

The PMMA holders are fabricated with a laser cutting machine (LaserScriber by Micro-la Optoelectronics s.r.l.), that defines the final geometry, the holes for the screws and the housings for the chip and gates.

Two different microfluidic structures were used in this work: one for the stability study and another one for the biosensing tests.

In the structure used for the stability tests, the gold gate is separated from the chip through the electrolyte in a vertical stack. Therefore, the chamber that hosts the electrolyte is composed by two complementary parts, as highlighted in [fig. 3.7 a)]. This design was chosen for its easiness of manipulation and reduced dimensions, allowing stable measurements over time and less engineering efforts prior its use.

For the sensing tests, the design used for the stability was not ideal for two main reasons.

Firstly, biosensing tests require maximum accuracy given the low concentrations of involved analyte. Thus, a differential measurements was mandatory to get rid of all the effects that could affect the quantification of the sensing tests, such as the drift of the transistor. To obtain that, a structure hosting a double gate was necessary, one exposed to the analyte and one acting as a reference.

Secondly, the design exploited for the stability test has only one chamber, which implies that the biomolecule to detect would eventually get in contact with the EGOFET. This fact can lead to unwanted doping of the semiconductor, which could influence the measurements and finally the quantification of the target to be analysed.

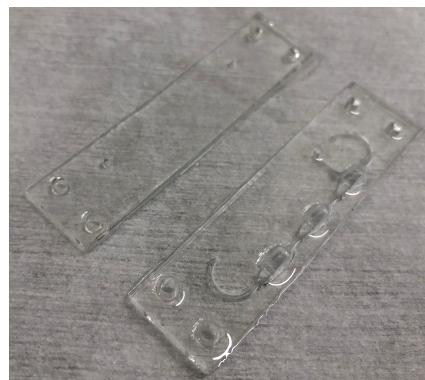
For these reasons, a new design was proposed [fig. 3.7 b)]. In this new configuration, there are two inlets (one for the main buffer and one for the analyte) and two gate electrodes for the differential measurements.

The outlet is placed near the functionalized gate in order to avoid contamination of the polymer by the analyte. This was confirmed by several simulations, taking into account the diffusion of Ang2 and different flow rates of the two solutions (not shown in this work).

The volume of each chamber is around $50 \mu\text{l}$ with an additional $30 \mu\text{l}$ for the inlet and outlet channels, so that for the vertical fluidics the total volume is around $80 \mu\text{l}$ while for the planar one the volume is around $200 \mu\text{l}$.



(a)



(b)

Figure 3.7: a) PDMS microfluidics for the vertical structure b) PDMS microfluidics for the double-gate planar structure

3.3 Measurement set-up

The measurement set-up for the experimental part can be conceptually divided in two areas: the electrical one and the fluidics.

The electrical contact of the device is provided by a probe station with three micro-manipulators that connect source, drain and gate electrodes with triaxial cables to the Source/Measure Unit (*Keysight B2912A*) [fig. 3.8]. Two channels are present; in this case the first channel (CH1) provides the voltage V_{DS} and measures the current I_{DS} , while the second one (CH2) provides V_{GS} and measures I_G , in a common source configuration. It supports coverage of 210 V, 3 A DC and 10.5 A pulse, and a minimum resolution of 10 fA and 100 nV.

The software *QuickIV* allows the configuration of the input signals and the processing of the output currents.



Figure 3.8: (a) Probe station (b) Keysight B2912A source/meter unit

For stability tests, the inlet of the device is connected to a syringe, driven by a syringe pump.

For sensing tests, since the device is equipped with two different inlets, one for the reagent solution and one for the washing solution, two instruments are required: a peristaltic pump drives the flow of analyte in the fluidics channel, while the syringe pump is devoted to the washing step [fig. 3.9].

The peristaltic pump working principle is based on a rotor that gradually compresses the tube and makes the solution flowing towards the sample. The pump used for this work is the ISMATEC IPC *High Precision Multichannel Pump* that provides four channels and

allows setting the flow rate, the flow direction and to start and stop the flux.

The syringe pump is the NE-4000 model from *KFTechnology*, able to control the flow rate from $1.5 \mu\text{l/hr}$ to 7515 ml/hr .

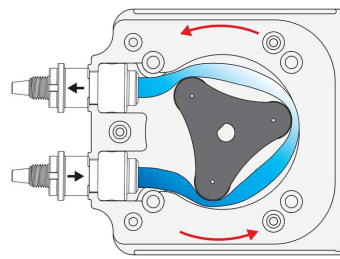
The whole setup is represented in [fig. 3.10].



(a)



(b)



(c)

Figure 3.9: (a) Peristaltic pump (b) Syringe pump
(c) Working principle of a peristaltic pump

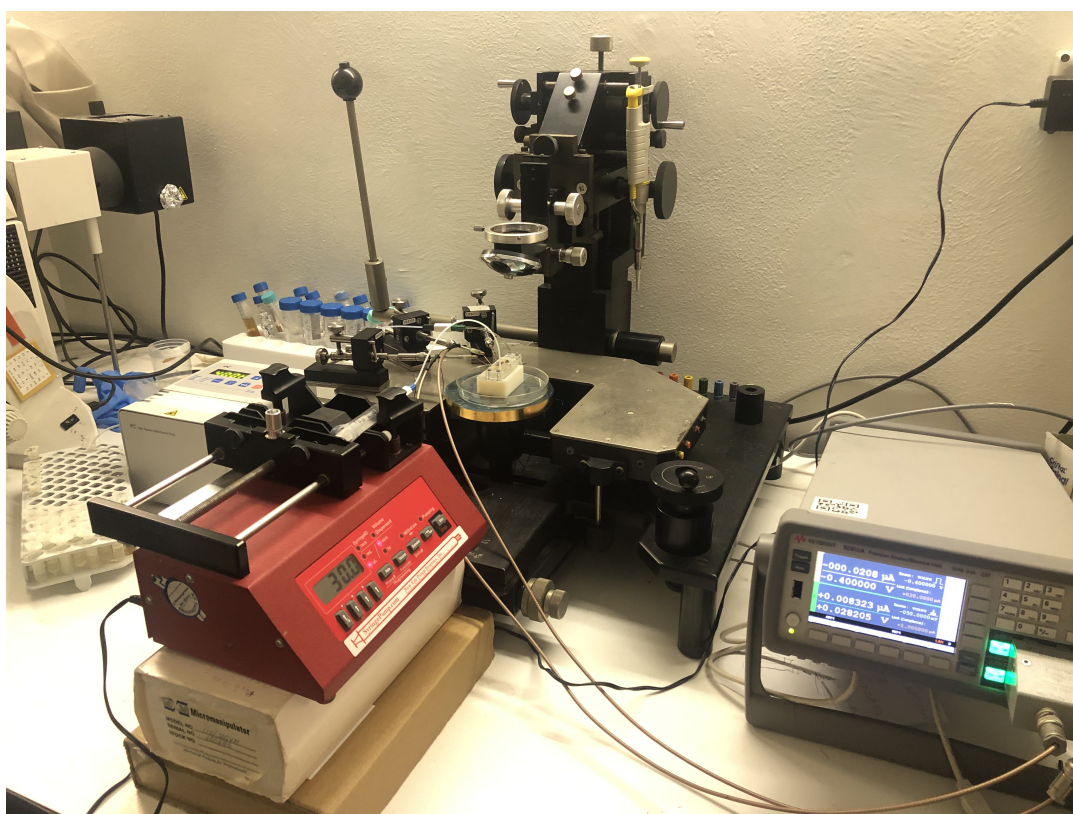


Figure 3.10: Experimental setup in Nanoscienze Lab, DISAT

3.4 Electrical characterization

The performances and the functionality of each device are investigated through electrical characterizations, aiming at extracting the most important figures of merit to properly describe the devices and eventually quantify the sensing of the analyte.

- **Output characteristic**

The output curves show the behavior of the channel current I_{DS} depending on the applied voltage V_{DS} for a fixed gate voltage V_{GS} .

The values used in this work are:

- for P3HT:

- V_{DS} sweeping from 0 V to -500 mV, forward and backward for each gate voltage applied;

- V_{GS} from 0 V to -800 mV with step of 100 mV;

- for P3CPT:

- V_{DS} from 0 V to -350 mV, forward and backward for each gate voltage applied;

- V_{GS} from 0 V to -600 mV with step of 100 mV

This characterization is important to distinguish the operational regimes of the device, in order to apply the proper voltage V_{DS} that assures the saturation condition when measuring the transfer characteristics and extracting the figures of merit.

In [fig. 3.11] an example of output curve of a device tested with *QuikIV* software is displayed.

- **Transfer characteristic**

The transfer characteristic shows the behavior of the channel current I_{DS} with the gate voltage V_{GS} , upon the application of a fixed V_{DS} that guarantees the saturation operational regime.

The values used in this work are V_{GS} sweeping from 0 to -600 mV and back and a fixed $V_{DS} = -400$ mV for P3HT and $V_{DS} = -250$ mV for P3CPT.

The values used in this work are:

- for P3HT:

- V_{GS} sweeping from 0 V to -600 mV, forward and backward for five consecutive times;

- fixed $V_{DS} = -400$ mV;

– for P3CPT:

V_{GS} from 0 V to -600 mV, forward and backward for five consecutive times;
fixed $V_{DS} = -250$ mV

From this curve it is possible to extract the two most important figures of merit discussed in this work, namely the threshold voltage V_{th} and the transconductance g_m (see section 2.1).

Practically, the transconductance is calculated as the maximum derivative of the $I_{DS} - V_{GS}$ curve, while the threshold voltage as the intercept with the x axis of the square root of the curve.

An example of a transfer curve is reported in [fig. 3.12].

- **Real time measurements**

During stability tests, the response of the device to the application of a continuous bias was also investigated.

Constant voltages of $V_{DS} = -400$ mV and $V_{GS} = -600$ mV for P3HT and $V_{DS} = -250$ mV and $V_{GS} = -600$ mV for P3CPT were continuously applied for a defined period of time (usually 10 or 20 minutes), then a transfer curve was recorded in order to monitor the effect of the bias on the degradation of the device performances through the extraction of the threshold voltage.

- **Pulsed measurements**

One of the main issues when dealing with forward and backward sweeps (as in this work) is hysteresis. Recently, new measurement protocols involving pulsed signals were suggested, which demonstrated to effectively reduce this phenomenon and decrease the gate current [65] [66]. For this reason, a similar protocol was exploited in this work during some stability tests and all sensing measurements. The voltage V_{DS} was pulsed with a pulse base of -400 mV and peak of 0 V, with a pulse width of 0.02 s, while V_{GS} has a more complex shape: a base voltage of -50 mV was fixed and the pulse peaks sweep from 100 mV to -600 mV, with a pulse width of 0.202 s. The shapes of the voltages are shown in [fig. 3.13] and a comparison of transfer characteristics obtained with the standard protocol and the pulsed one is reported in [fig. 3.14], where the hysteresis is noticeably reduced.

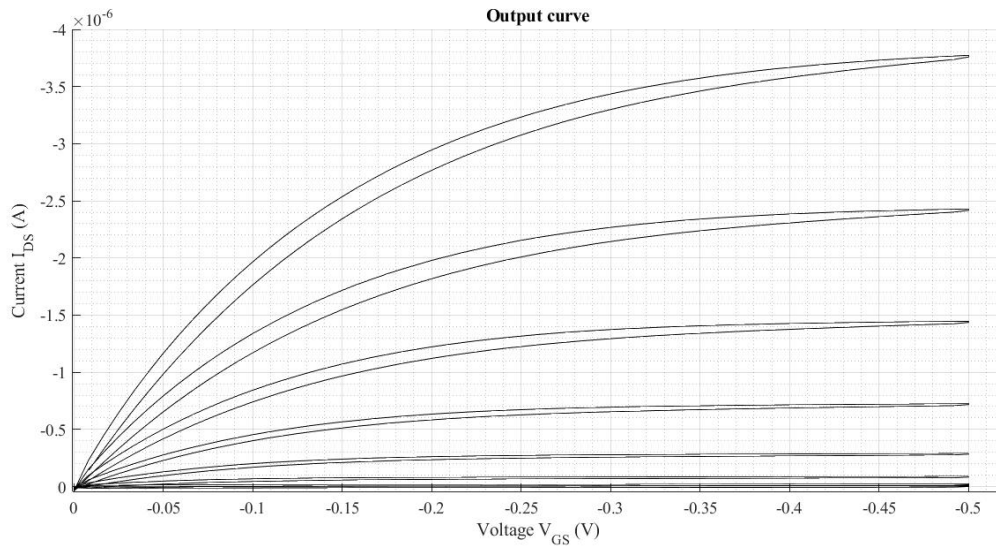


Figure 3.11: Output curve of a tested device

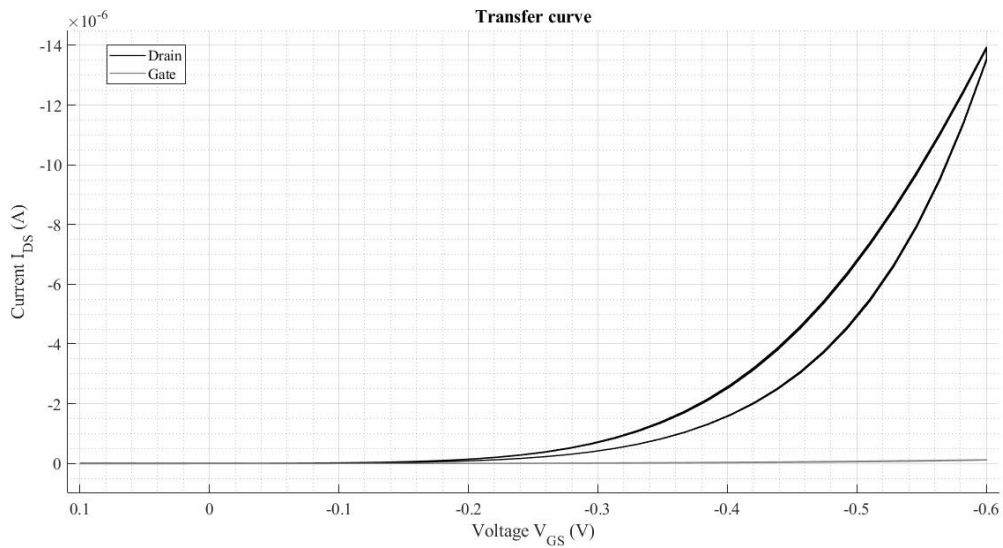


Figure 3.12: Transfer curve of a tested device

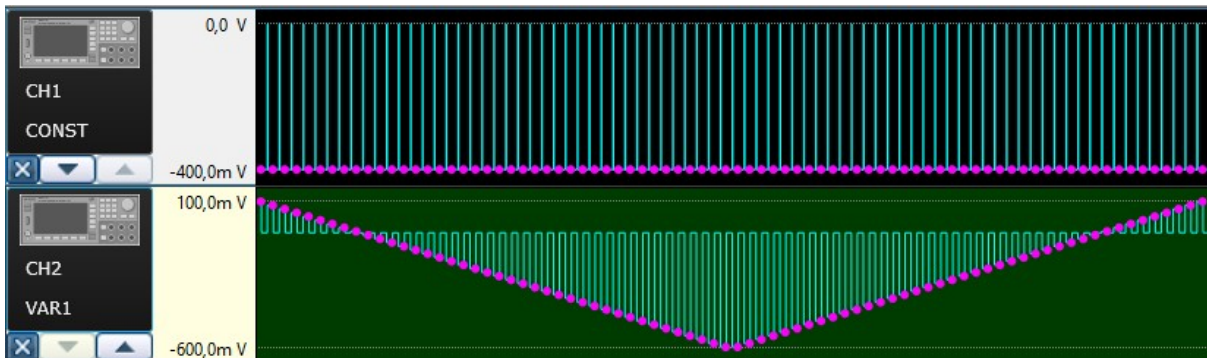
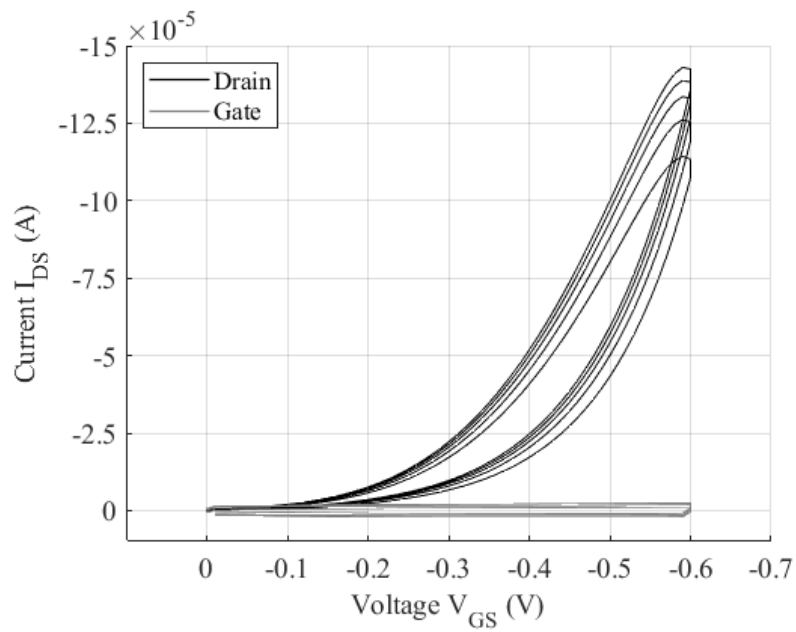
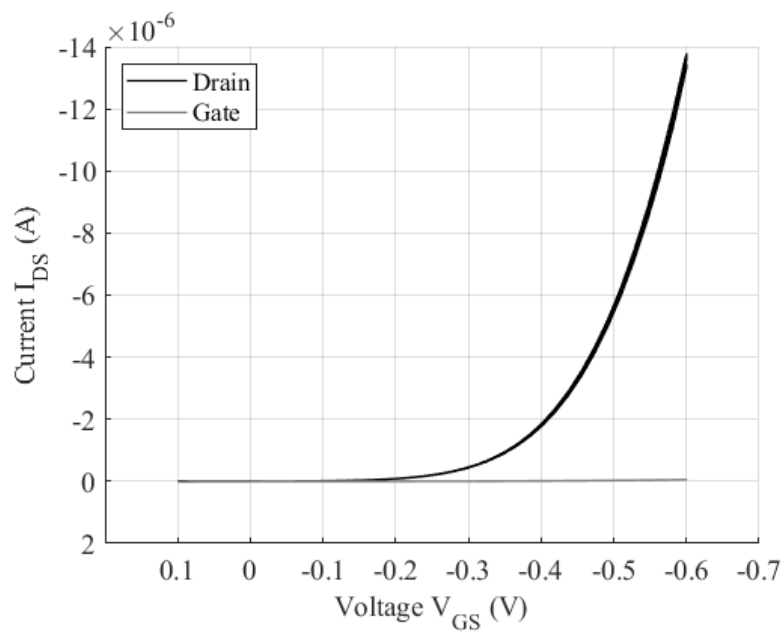


Figure 3.13: Pulsed protocol by *QuikIV* software



(a)



(b)

Figure 3.14: a) Transfer curve obtained with the standard measurement protocol b) Transfer curve obtained with the pulsed measurement protocol

3.5 Experimental protocols

3.5.1 Stability tests

The stability over time was investigated according to different experimental conditions, such as:

- Effect of the applied bias on the device;
- Effect of storage under vacuum.

Therefore, some devices were assembled and tested right after the fabrication (referred as "*fresh*"), while others were stored in a vacuum dryer, then assembled and tested the day after (referred as "*old*").

In both cases, the measurement protocol was the same: the device was filled with PBS 1x and connected to the source/meter through the micromanipulators on the probe station; then the electrical characterization were performed.

First, an output curve and a preliminary transfer curve are taken to assess the performances of the device.

Then, only one of the three devices on the chip is subjected to a continuous measurement (referred as "*bias*"), while on the other two devices the transfer characterization is performed at different times.

A further continuous monitoring of the stability was also performed by measuring 100 transfer curves on a device in two different times. This measure was done in order to further investigate the charge trapping phenomenon exhibited by the OSCs and their recovery ability after a rest period. In this case, only one device is interested by the measure and the pulsed protocol was chosen, since much more stable curves can be obtained.

3.5.2 Sensing tests

Two types of sensing tests were performed: one involving the BSA, whose aim was the validation of the fluidics, and a second one involving Ang2.

In both case, the measurements follow the same steps.

All the devices were stored in PBS and in dark and were assembled and tested one day after their fabrication.

When the vertical structure was employed, mainly for the first BSA sensing tests, a functionalized gate was inserted above the PDMS structure, so that a small area of 9 mm^2 was exposed to the electrolyte. The inlet of the structure was connected to the peristaltic pump, which pulls the fluid inside the device.

After the preliminary transfer measurements, a first transfer curve with only PBS is taken (*Blank* measurement).

Then, PBS with increasing concentration of BSA flows into the device and the transfer curves are measured, according to the following protocol:

- The device is filled with the first BSA concentration;
- an incubation time of 15 minutes is observed, in order to let binding events occur;
- a washing step is done by inserting PBS only, to get rid of any non-specific absorption on the gate functionalized surface;
- the transfer curves are measured on each of the three devices on the chip.

Then, the next BSA concentration is inserted in the device and the protocol starts over again.

Few sensing experiments were performed with this vertical structure, since the risk for contamination for the polymer surface was very high. This reason, along with the ones already explained, led to the design of the double-gate planar fluidics.

Also in this case, the preliminary transfer curves and the blank measurements are performed after the assembly of the device with one functionalized gate and one bare gold gate. The exposed areas are the same as before, i.e. 9 mm^2 . The protocol is the following:

- The peristaltic pump drives the solution of analyte (BSA or Ang-2) inside the device from the inlet near to the functionalized gate. Since the outlet is positioned under the functionalized gate, contamination of the polymer with the analyte is avoided;

- the incubation time of 15 minutes is observed;
- the syringe pump drives the PBS in the device from the opposite inlet, near to the bare gold gate, for the washing step;
- the transfer curves are measured for each of the three devices on the chip, both with the functionalized gate and the reference bare gate.

Then, the next target concentration is inserted in the device and the protocol starts over again.

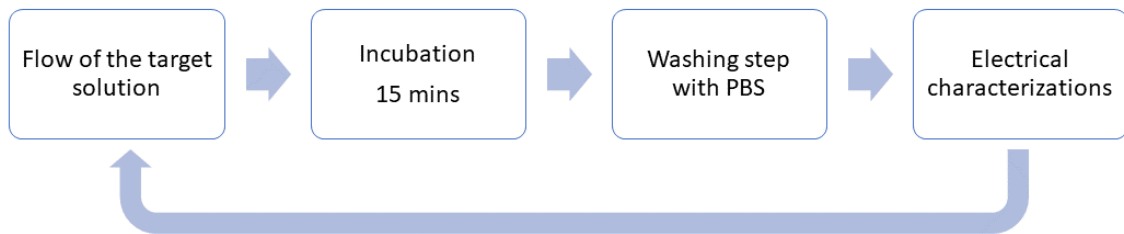
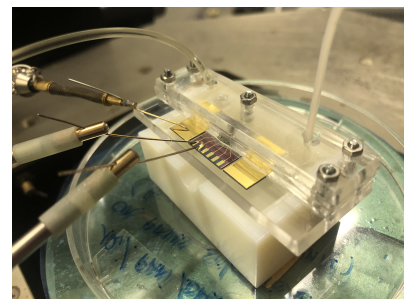


Figure 3.15: Process flow of sensing measurements



(a)



(b)

Figure 3.16: a) EGO-FET vertical structure during a stability test measurement
b) EGO-FET double-gate structure during a sensing test measurement

Results and discussion

This chapter deals with the main experimental results found in this work. In the first part of the chapter, the results of the stability study will be presented with a discussion on the different impact of the electrical bias stress on the two polymers, while in the second section the data about biosensing experiments involving Ang-2 detection will be shown.

4.1 Stability results

Before any attempt of biosensing application, it is necessary to assess the reliability of the device by investigating its stability in time.

The effect of storage on the polymer performances and the degradation causes are poorly understood. Stability of organic materials in different environmental conditions has been explored in a general way, mostly regarding different polymers with respect to the ones used in this work [67] [68]. Instead, the response of OSC to an electrical bias stress has been more extensively reported in OFET, even though the physical mechanism underneath the consequent degradation of the polymer is not yet fully explained and the presence of electrolyte has not been addressed.

For this reason and given the proposed application to provide a disposable device for the POC (Point of Care) framework, it is important to carry out a deeper stability study and to define the best conditions of storage and operation for the biosensor.

The task was achieved by monitoring the behavior of the device in the different conditions described in section 3.5.1, i.e *fresh* (used right after fabrication), *old* (stored one day in vacuum before measurements) and *bias* (used right after fabrication with an application of a continuous bias).

Since each fabricated chip presents three different devices, the figures of merit extracted from each measurement on each device were averaged.

The time evolution was monitored by sampling on 10, 20, 40, 70, 100, 300 and 1000 minutes, so that every measurement performed outside these values was aggregated to the corresponding nearest value. All the variations are normalized to the first measurement.

Storage

The effect of the storage in vacuum on the device performances is presented in [fig. 4.1] and [fig. 4.2].

The variation of the threshold voltage ΔV_{th} was calculated as:

$$\Delta V_{th,i} = \frac{V_{th,i} - V_{th,0}}{V_{th,0}}$$

where the index 0 stands for the first measurement and the index i stands for the following ones. The same formula holds for the variation of the transconductance g_m .

Since both polymers are p-type, they are characterized by negative threshold voltages. This means that:

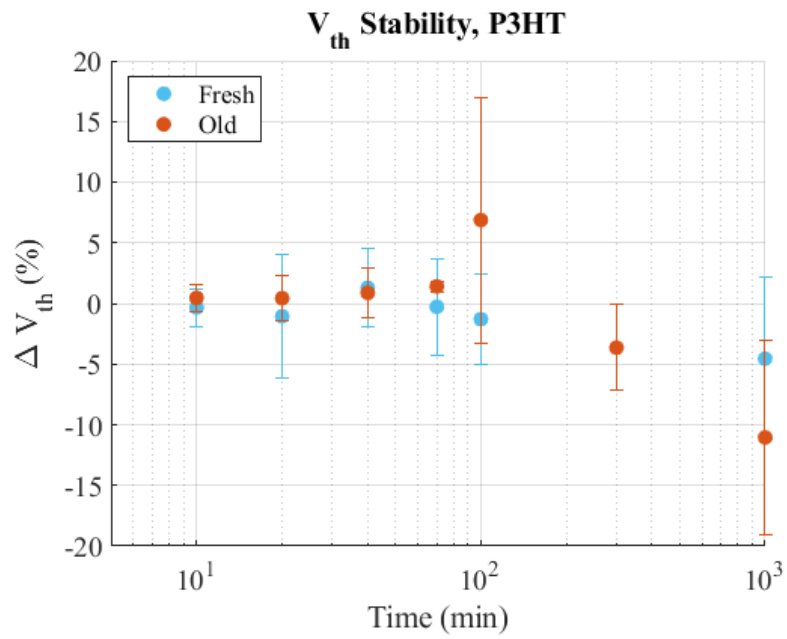
$$\Delta V_{th,i} < 0 \rightarrow |V_{th,i}| < |V_{th,0}|$$

$$\Delta V_{th,i} > 0 \rightarrow |V_{th,i}| > |V_{th,0}|$$

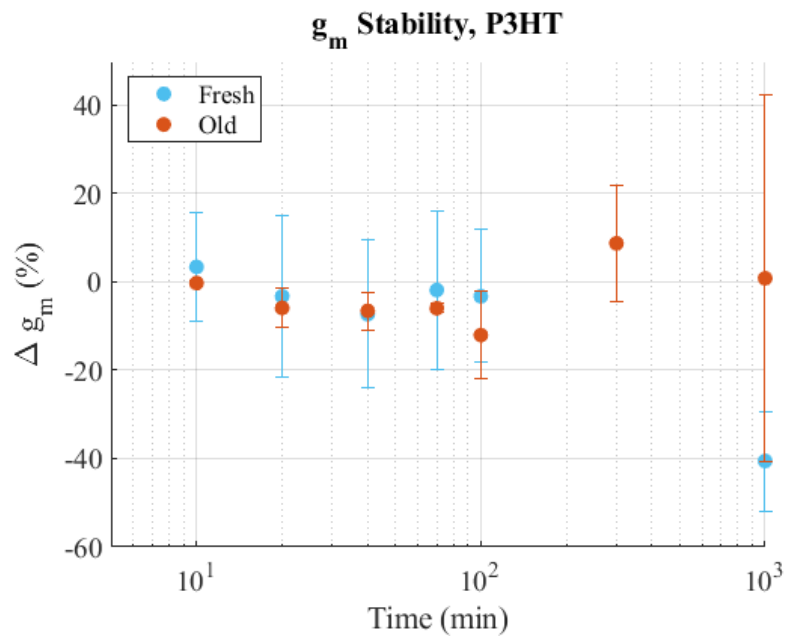
In the first case, the threshold voltage (in absolute value) is decreasing and the device is always easier to switch ON; in the second case the threshold voltage is becoming more and more negative, so the device is progressively harder to switch ON since a higher $|V_{GS}|$ is needed.

Similarly for the g_m : $\Delta g_m < 0$ means that the transconductance is decreasing while $\Delta g_m > 0$ stand for an increasing transconductance, which makes easier the flowing of carriers in the polymer.

As depicted in [fig. 4.1], P3HT appears very stable in time: the threshold voltage of *fresh* devices presents a quite stable variation of $[-5\%, +5\%]$ for a fairly long period. The storage in vacuum (*old*) seems to have no visible effect on the threshold voltage unless for longer testing times, i.e. 10^3 minutes, when a slight worsening of the performances appears.

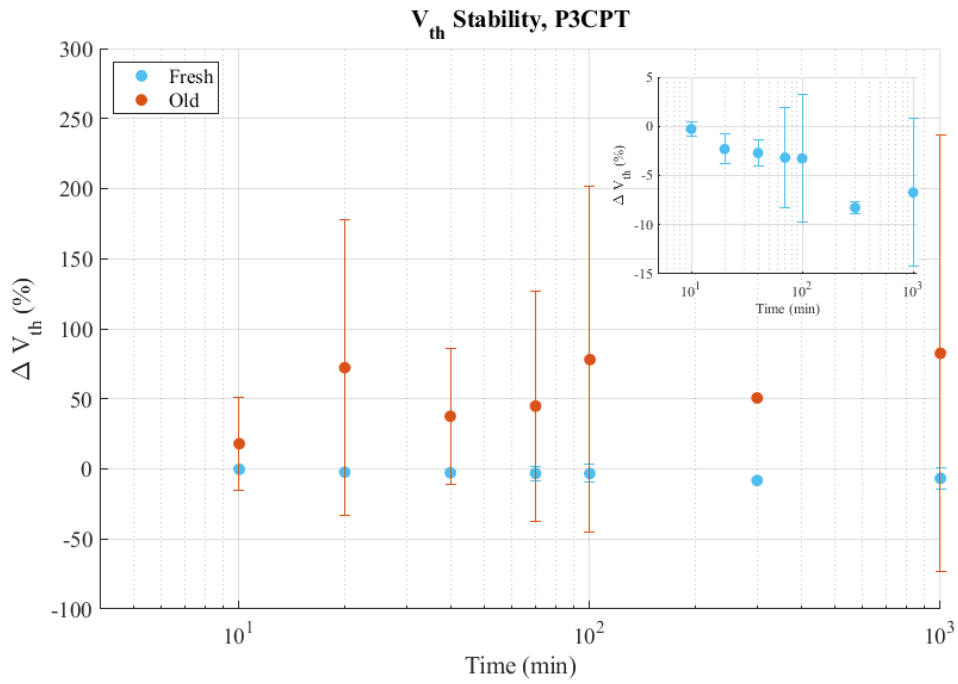


(a)

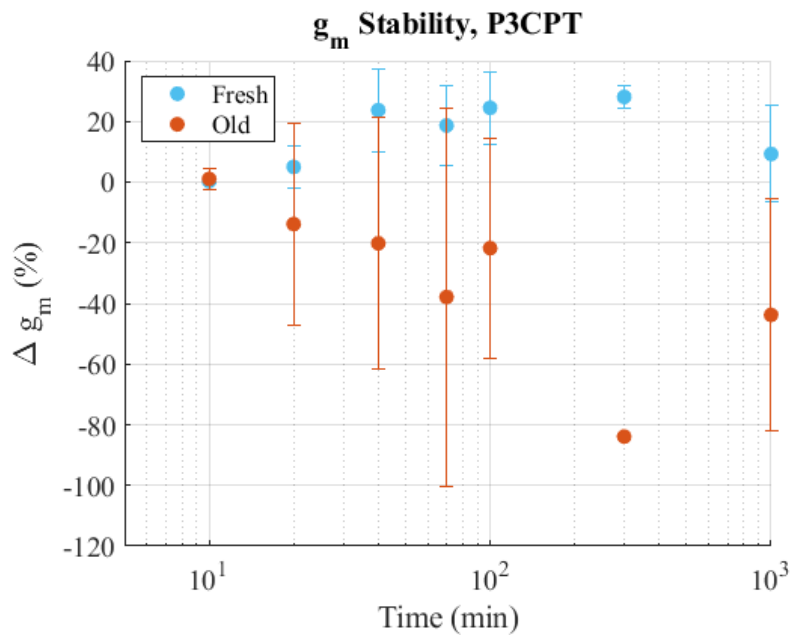


(b)

Figure 4.1: Effect of storage in vacuum on a) the threshold voltage V_{th} and b) the transconductance g_m for P3HT-based devices



(a)



(b)

Figure 4.2: Effect of storage in vacuum on a) the threshold voltage V_{th} and b) the transconductance g_m for P3CPT-based devices

The transconductance presents a much wider variation Δg_m of about $[-20\%, +20\%]$. Nonetheless, similar values are found for *old* devices, confirming the little effect of storage condition on P3HT.

Again, when approaching longer measuring times, a worsening of the performances appears both for *fresh* and *old* devices, suggesting a natural degradation of the polymer.

Fresh P3CPT presents slightly wider variations of the threshold voltage with respect to P3HT: ΔV_{th} falls into $[-10\%, +5\%]$ for a time period of about 5 hours as highlighted in the inset of [fig. 4.2]. The most important thing is that storage has a very dramatic effect on P3CPT threshold voltage: mean variations of more than $+50\%$ occur already at few tens of minutes of testing, with very large dispersion. As anticipated before, this means that V_{th} is becoming more and more negative, thus increasing the V_{GS} needed to turn the device ON.

This is also reflected by a negative shift of the transconductance g_m : in the *fresh* condition Δg_m tends to stabilize to about 30% , while in the *old* condition a rapid and very large reduction of g_m is observed, meaning that the transport of carriers in the channel is more and more difficult.

These results suggest that in general storage in vacuum can lead to a decrease of the performances of the EGOFET, that is much more evident in P3CPT-based devices for which an alternative storage method has to be found.

The literature about polymers' stability ^[69] ^[54] suggests that the exposure of the polymer to dry air and even vacuum is more detrimental than water or humidified air.

Sirringhaus ^[69] proposes a drift of the negative ions of water towards the active interface in the latter case, that should lead to an accumulation of positive charges in the OSC layer and thus to an improvement of the carrier transport, while the degradation in vacuum and dry air was ascribed to a not better specified charge trapping phenomenon at the polymer surface.

According to these considerations, the different impact of vacuum exposition on the two polymer could be due to the intrinsic properties of P3HT and P3CPT: the polarity of the P3CPT side chains and its hydrophilic nature could make it more prone to permeation by water molecules, so it is possible that the absence of this environment has a more pronounced effect on its performance rather than on P3HT's one.

Electrical Bias

It is known that for p-type OSC, an electrical bias stress results in a negative variation of the threshold voltage ^[69] (that is $V_{th,1} - V_{th,0} < 0 \rightarrow |V_{th,1}| > |V_{th,0}|$) and again many studies ascribed this behavior to a charge trapping phenomenon at the interface of the polymer ^{[54] [70] [71]} or to proton migration phenomena ^[72]. More specifically, the application of a gate voltage $V_{GS} < 0$ leads to a build-up of mobile negative charges at the OSC interface, that have to be compensated by the subsequent V_{GS} before the accumulation layer can be formed and the same current values of the previous situation can be reached ^{[73] [74]}.

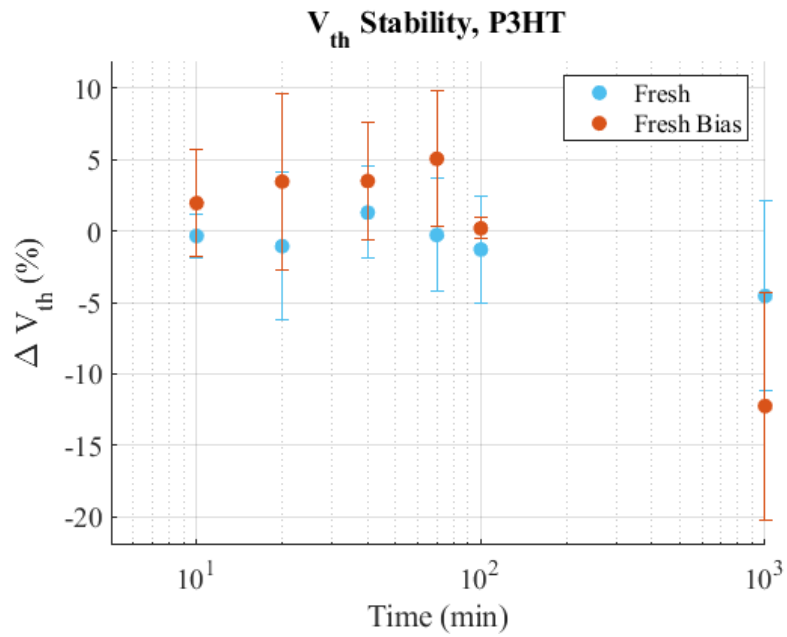
In this work, the effect of the electrical bias stress was also investigated and the results are reported in [fig. 4.3] and [fig. 4.4]: the threshold voltage and the transconductance of the device are measured after a cycle of continuously applied constant bias and then compared to the *fresh* situation.

When dealing with P3HT, the main effect of the bias stress seems to be an almost constant shift of the threshold voltage towards higher values. In fact, the ΔV_{th} of *bias* devices depicted in [fig. 4.3] seems to follow the same trend of the *fresh* condition with a shift of about 5%.

The same observation holds true for the transconductance g_m : upon a 15% – 20% shift towards lower values, the followed trend in time seems to be very similar to the *fresh* situation. Also, the total behavior is consistent between the two quantities: a reduction of g_m is correctly reflected to an increase of the V_{th} , meaning that higher effective V_{GS} are required to achieve a specific operational point when dealing with *biased* devices.

Again, when approaching longer times, greater variations of both figures of merit occur, but it is no more possible to distinguish if the performance decrease is due to the bias effect or to the natural degradation of the polymer.

Concerning P3CPT, a much more detrimental effect is observed: [fig. 4.4] shows large positive variations of the threshold voltage with huge dispersion and a rapid decrease of the transconductance with larger dispersion with respect to P3HT, suggesting that P3CPT is much more sensitive to bias stress.



(a)

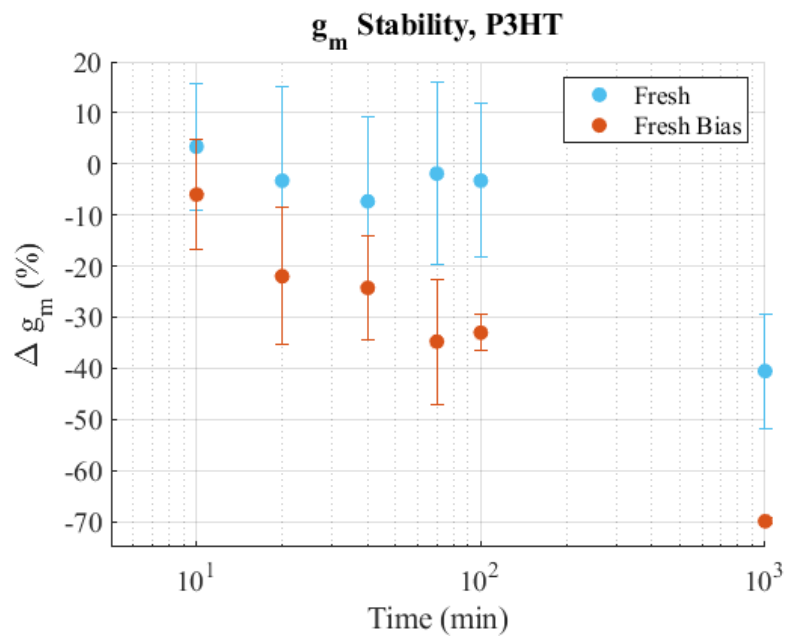
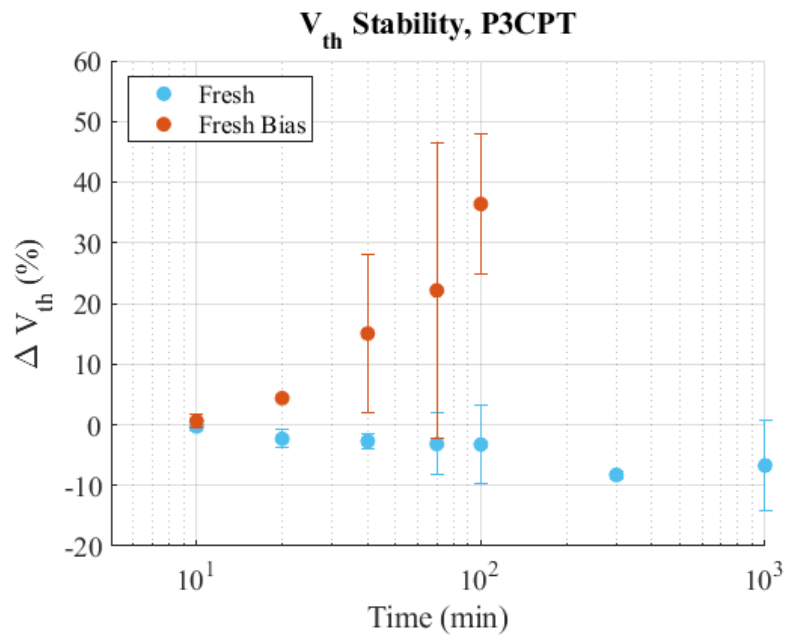
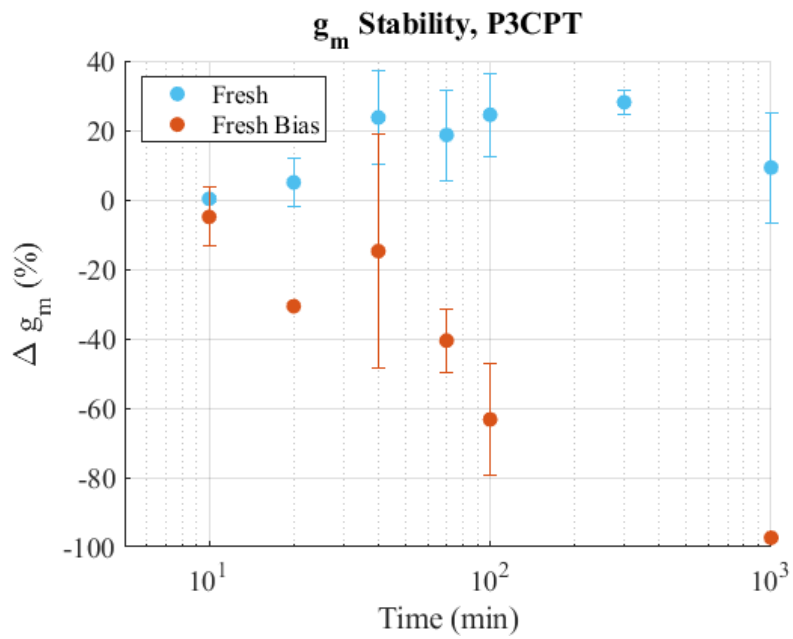


Figure 4.3: Effect of an applied bias on a) the threshold voltage V_{th} and b) the transconductance g_m for P3HT-based devices



(a)



(b)

Figure 4.4: Effect of an applied bias on a) the threshold voltage V_{th} and b) the transconductance g_m for P3CPT-based devices

Differently from P3HT situation, while the *fresh* figures of merit tend to stabilize in time, in the *biased* device this never happens. Indeed a continuous degradation of the performance occurs, suggesting the action of some progressive phenomenon such as the formation of some trap states in the polymer.

Unfortunately, the origin of these trap states in organic materials is still to be found, since it is not yet clear whether they arise from structural defects or chemical reaction with oxygen or moisture [75]. The influence of water in molecules in the degradation of some OSC was also proven [76], but it doesn't seem to be the case of this work since P3CPT proved to be very stable when in contact to an aqueous electrolyte without any external stress. Indeed, storage in vacuum and electrical stress have almost the same impact on the P3CPT performances, so the most reasonable hypothesis is that the prolonged application of the bias could enable some worsening phenomenon: Raman analyses on P3CPT surface of *biased* devices (not reported in this work) highlighted an oxidative process on the polymer, probably enhanced by the hydrophilicity of P3CPT that makes easier the penetration of water molecules or oxidant ions.

In order to better understand the mechanism leading to the bias stress instability, a different test was performed on both polymers. The devices were subjected to two cycles of continuous measurement of 100 transfer curves, with a pausing time between them of about one hour. Then, V_{th} and g_m were extracted and they are reported in [fig. 4.5] and [fig. 4.6].

It is very interesting to notice that the two polymers have completely different behaviors, both in the evolution of V_{th} and g_m during the bias stress and after the rest period, when the recovery of both V_{th} and g_m is almost perfect for P3HT, while P3CPT does not recover the initial performances but keeps behaving such as the rest period was not observed.

The negative ΔV_{th} and the positive Δg_m for P3HT mean that carriers are increasing, so an improvement of the performances is occurring.

This last remark is suggesting that the electrical bias could induce a polarization of the polymer rather than a charge trapping phenomenon. P3HT is known to form a reversible charge-transfer complex with oxygen [69] [77] [54], that eventually leads to the formation of a mobile hole in the backbone of the polymer [54]. This phenomenon was proven to facilitate the generation of carriers especially upon application of an electric field across the polymer [77].

This suggestion could well explain the shift of V_{th} towards lower values, since an increase of the carrier concentrations leads to a lower effective V_{GS} to apply in order to get a specific point of operation.

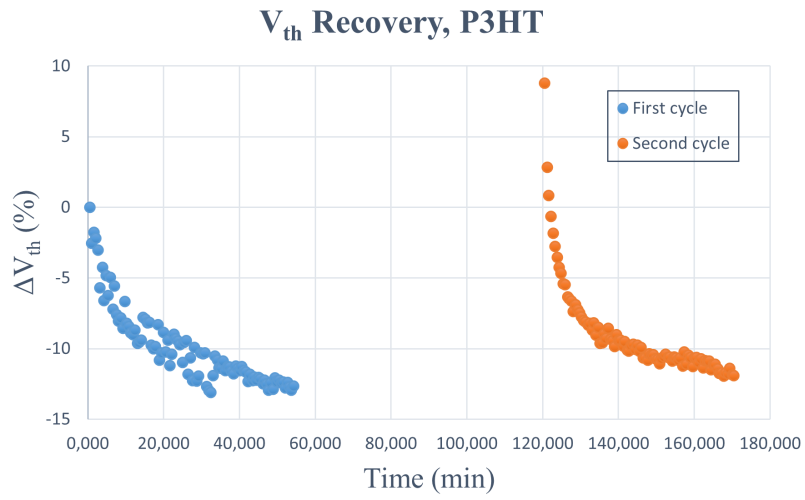
The recovery of the performances after the non-operating period, already mentioned in literature ^[78] ^[69], is also clear and strengthens the hypothesis for a reversible polarization phenomenon.

A completely different situation is depicted for P3CPT, for which the rest period does not restore the initial conditions: the device seems to maintain the polarization acquired with the application of the first bias and keeps following the same trend when the second bias is applied, as it is better shown in [fig. 4.6].

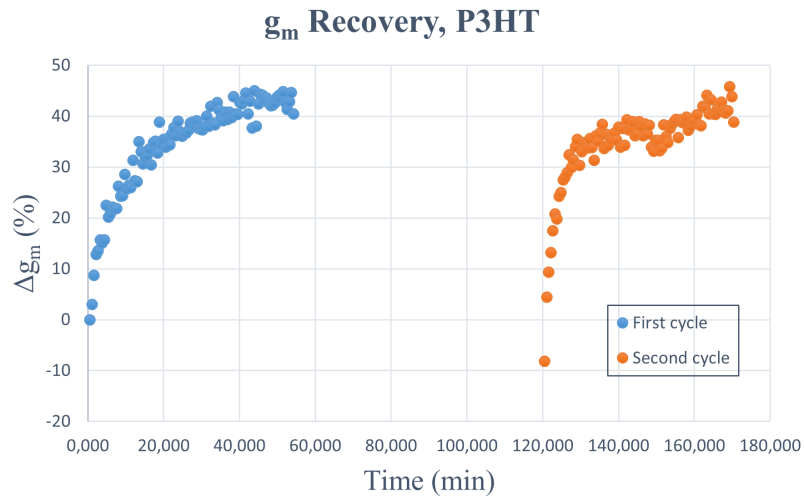
In this case, the suggestion of the charge trapping phenomenon of P3CPT ^[52] seems to be confirmed: the negative charges are trapped at the OSC/electrolyte interface, modifying the surface potential and thus modifying the threshold voltage. Moreover, these negative charges would induce electrostatic repulsion with the ionic species of the electrolyte, resulting in a weakened EDL formation that leads to the decrease of the performances of the device ^[79].

It is possible that the process of charge trapping for P3CPT could involve bulk states rather than superficial ones (i.e. charges are stored inside the bulk of the semiconductor)^[52]; this assumption could explain the wide variations observed and the divergence between the trends of *fresh* and *biased* devices.

Very likely, only an opposite polarized voltage could restore the neutral condition, as also mentioned in literature ^[69].

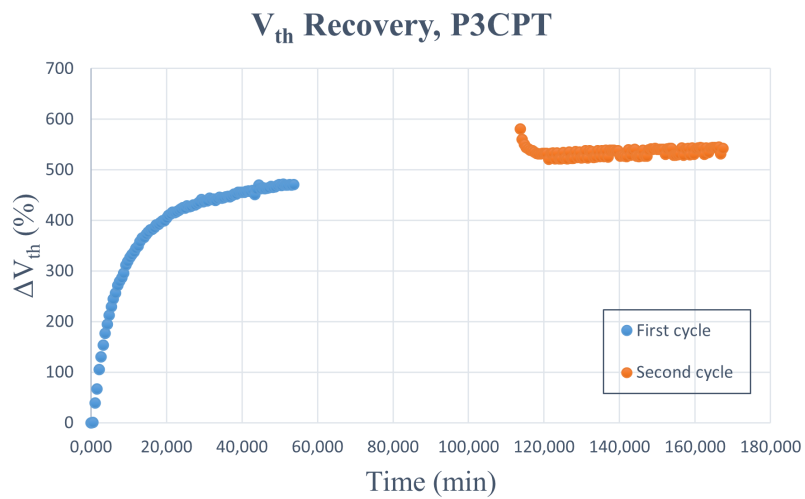


(a)

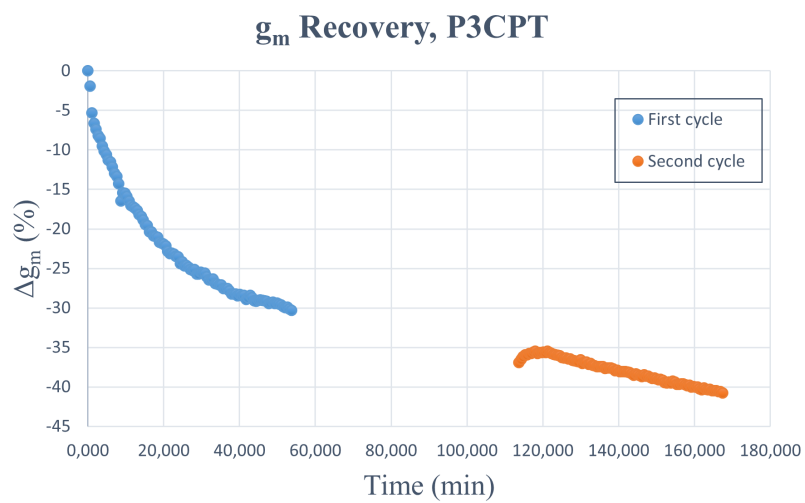


(b)

Figure 4.5: Recovery of a) the threshold voltage V_{th} and b) the transconductance g_m of P3HT after a rest period of 1 hour



(a)



(b)

Figure 4.6: Recovery of a) the threshold voltage V_{th} and b) the transconductance g_m of P3CPT after a rest period of 1 hour

4.2 Sensing results

After assessing the stability of the device for a reasonable temporal window, sensing experiments were performed with two different analytes: BSA for the device validation and Ang-2 for the effective device application.

As already anticipated, all the devices were stored one day in PBS before the assembling to guarantee stable performances.

4.2.1 Device validation: BSA sensing

A first sensing test involving BSA was performed on both polymers, exploiting mainly the double-gate planar microfluidic structure. In this case, differential measurements were performed: for each of the three devices on an EGOFET biosensor the threshold voltage and the transconductance were extracted by recording transfer curves both with the functionalized gate and the bare gold gate for each target concentration. Then, the variation of the difference between the two quantities was monitored:

$$\begin{aligned} V'_{th} &= V_{th} - V_{th,ref} \\ \Delta V'_{th} &= \frac{V'_{th,i} - V'_{th,0}}{V'_{th,0}} \end{aligned}$$

where the index i stands for the measurements at different concentrations of the analyte and the index 0 stands for the blank measurement acting as reference. All values are considered in absolute value, so that an increase of the Δ corresponds to an increase of the i -th quantity with respect to the blank. The results are reported in the following.

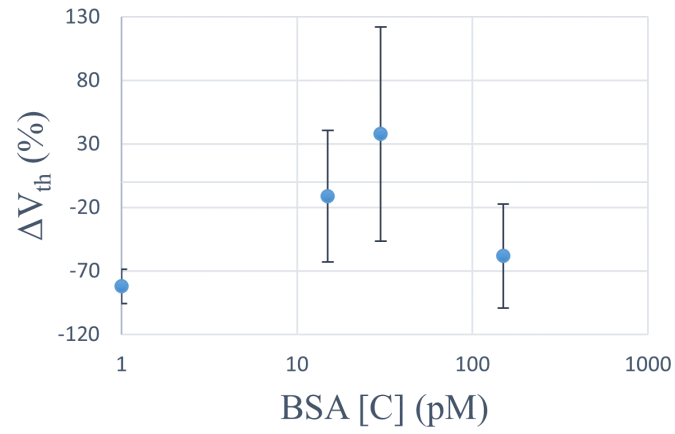
As shown in [fig. 4.7], for the P3HT-based devices a first important variation is recorded with respect to the blank condition: a shift of about 100% occurs for both V_{th} and g_m already at 1 pM concentration of BSA. Unfortunately, for all the other analysed concentration, the mean variation does not present a defined behavior and the dispersion of both values is high, denoting high instability and a not guaranteed replicability of the measurements. The sensing of the BSA therefore cannot be proven.

A possible explanation is the low capacitance of the P3HT. In fact, as already seen before, the total capacitance of the EDL formed on the two interfaces can be decomposed in:

$$\frac{1}{C_{tot}} = \frac{1}{C_{OSC}} + \frac{1}{C_G} \quad (4.1)$$

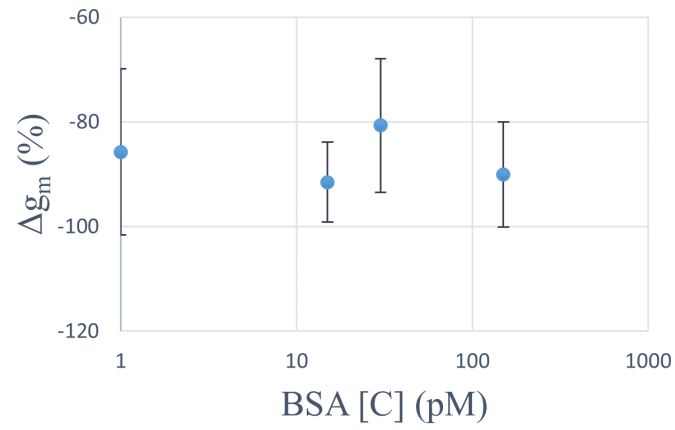
where C_{OSC} is the capacitance of the polymer and C_G is the capacitance of the gate.

V_{th} variation, P3HT



(a)

g_m variation, P3HT



(b)

Figure 4.7: Variation of a) V_{th} and b) g_m for P3HT-based devices

In the series of capacitances, the one prevailing is the smallest between the two, which in this case is C_{OSC} . Therefore, any variation on the gate capacitance cannot be detected since $C_G > C_{OSC}$.

This hypothesis is confirmed also by the g_m variation in [fig. 4.7]: it seems to stabilize to a variation of 90%, very close to the initial one. As demonstrated in section 2.1, the transconductance depends on the mobility of the carriers and the capacitance of the polymer. Assuming that C_{ox} is not changing, since the contamination of the polymer is avoided thanks to the double-gate microfluidic structure, also the carrier mobility is not changing so carriers are not affected by the progressive binding events between BSA and the anti-BSA layer on the gold surfaces.

Instead, when dealing with P3CPT, more promising results were obtained. The graph in [fig. 4.8] shows consistent variations of the differential V_{th} and g_m (well beyond the natural drift variations observed in stability tests) corresponding to different concentrations of BSA.

These results confirm the above discussion: it is known the capacitance of P3CPT is higher than P3HT^[52] so, in the series of the capacitance as in [eq. 4.1] it is very likely that C_G has a major impact rather than C_{OSC} , allowing the detection of binding events on gold surface.

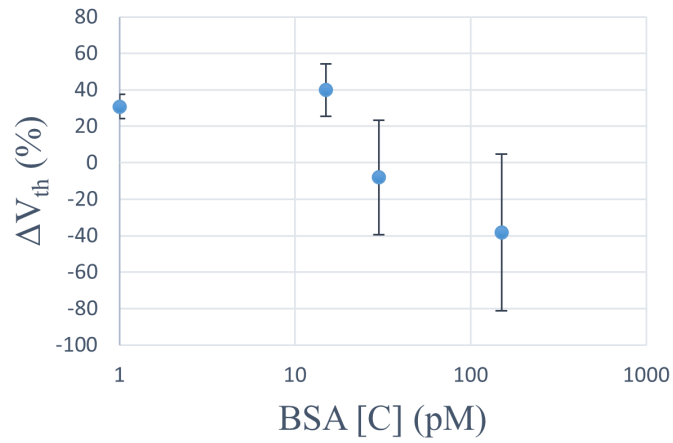
The isoelectric point of BSA is 4.9^[80], meaning that it provides negative charges when dispersed in a neutral medium. Knowing this, the expected effect of binding events should be an enhancement of the device performances, with an increase of the output current. Instead, the measurements give the opposite results as shown in [fig. 4.9].

According to Torsi's sensing model^[4], the changes in the electrical quantities due to binding events can be decomposed in two contributions: the additional charges provided from the target affect the variation of the threshold voltages, while the changes in the capacitance due to the formation of an additional layer of molecules affect the variation of the transconductance g_m .

The obtained results can be explained with the combination of the two effects above. I_{out} decreases following g_m , being the latter its derivative. A decrease in g_m should indicate a decrease in the capacitance C , that also affects the threshold voltage since $V_{th} \propto \frac{1}{\sqrt{C}}$, so $|V_{th}|$ increases, as initially occurs.

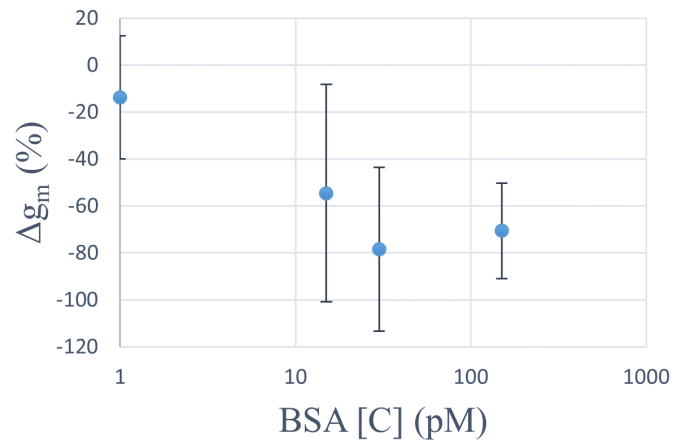
Anyway, the progressive addition of BSA leads to accumulation of negative charges,

V_{th} variation, P3CPT



(a)

g_m variation, P3CPT



(b)

Figure 4.8: Variation of a) V_{th} and b) g_m for P3CPT-based devices

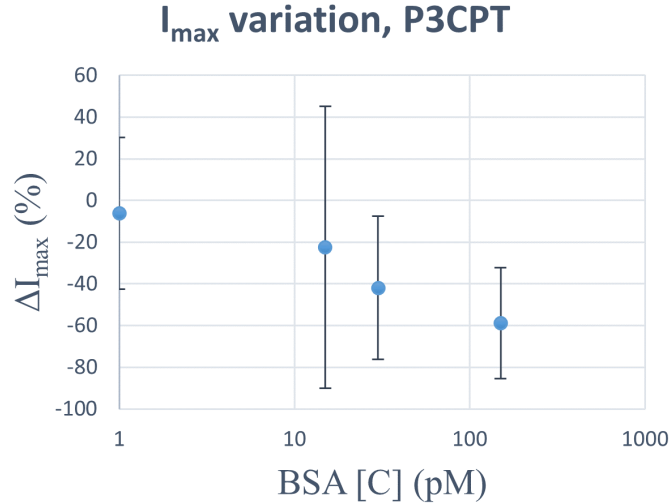


Figure 4.9: Variation of the maximum output current I_{max} for P3CPT-based devices

that only affects the variation of the threshold voltage and overcomes the effect of the capacitance. Thus, when increasing the BSA concentration, V_{th} is correctly decreasing but the effect of the decreasing capacitance on g_m leads anyway to a decrease in the current.

4.2.2 Angiopoietin-2 sensing

The sensing tests with Ang-2 were performed using P3CPT-based EGOFETs. This choice was justified by the previous considerations arisen from the BSA sensing and further confirmed by a preliminary test on P3HT which did not provide particularly relevant results [fig. 4.10].

The results obtained from the P3CPT-based devices are not very easy to interpret. Many tests were performed and a common behavior among all the devices was hard to find.

Some promising results were collected and an example is depicted in [fig. 4.11].

High variations beyond the stability recorded ones are observed for both the threshold voltage and the transconductance, already at very low concentrations of Ang-2 such as 0.1 pM and 0.5 pM, with a visible trend following the increasing concentrations.

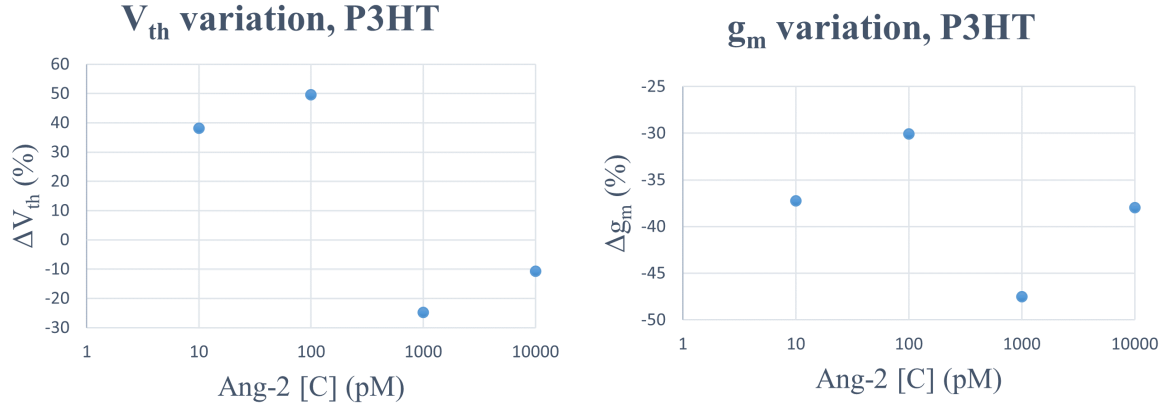


Figure 4.10: Preliminary Ang-2 sensing test on P3HT: the detection of the analyte cannot be proven

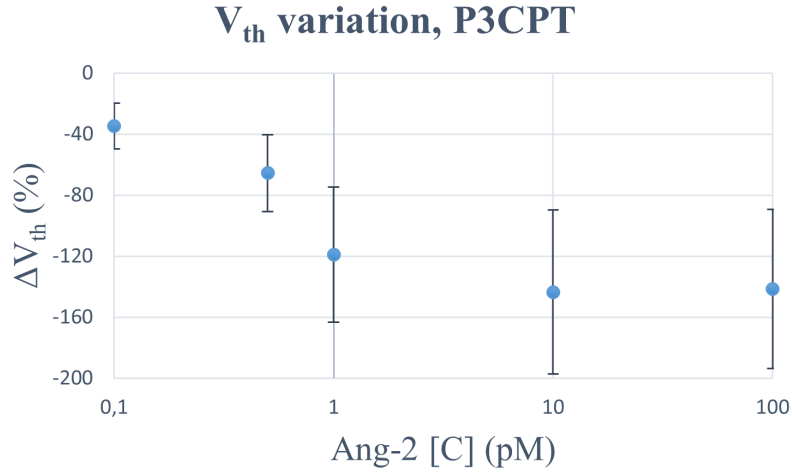
The more and more negative variation of the ΔV_{th} is denoting that the device is progressively easier to switch ON; also the transconductance of the device is increasing with increasing Ang-2 concentrations.

The layer of target-antibody on the gate surface is therefore changing the capacitance C_G and modifying the surface potential, probably by increasing the surface negative charge and leading to a greater accumulation of positive charges in the OSC channel, which in turn allows a much more efficient carrier transport, well represented by the increasing output current ([fig. 4.12]).

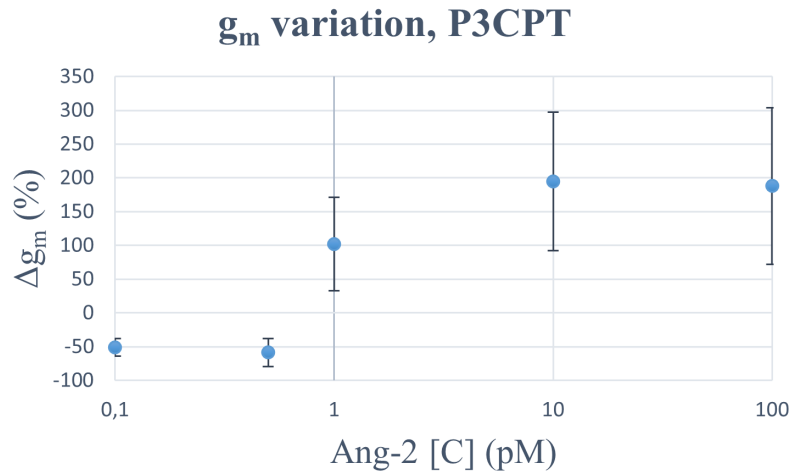
When approaching higher concentrations, a plateau is characterizing all the analysed quantities. This could be indicative of the saturation of the available binding sites on the surface of the gold gate, so that every increasing concentration is unable to produce further variations.

These very promising results perfectly match the expectations: the isoelectric point of Ang-2 is known to be 5.5 – 6 [81] meaning that, when dispersed in a neutral buffer as the used PBS is, it should expose a negative charge. Therefore, the effective voltage V_{GS} applied on the gate results higher and leads to a smaller V_{th} in modulus.

From the above analysis, the optimal range of detection results to be [0.1, 10] pM, which perfectly fits the purpose of this work: concentrations from 25 pM to about 45 pM of Ang-2 have been recorded in lung cancer patients, depending on the stages of the tumor [1], so it is very likely that the detection of lower amounts of Ang-2 could improve the chances for the *early* diagnosis.



(a)



(b)

Figure 4.11: Variation of a) V_{th} and b) g_m of a P3CPT-based EGOFET during an Ang-2 sensing test. A common trend is noticeable

On the other hand, several tests have provided discouraging results since they do not allow the recognizing of some binding events. Unfortunately, this is representative of poor replicability of the results and brings out the need for a more in-depth understanding of the sensing mechanism and a more efficient manufacturing of the device.

A quite random behavior of the figures of merit was recorded ([fig. 4.13]) and in some cases the behavior is opposite to the one previously described: the variations are positive, meaning that the threshold voltage is progressively higher and the device is harder to switch ON ([fig. 4.14]).

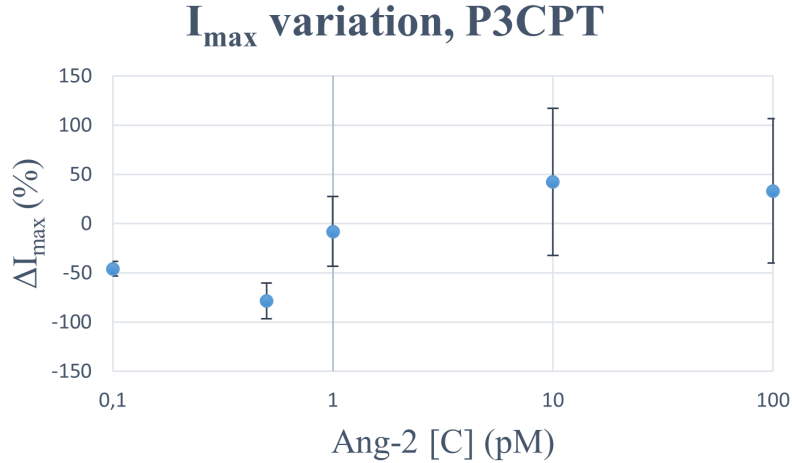
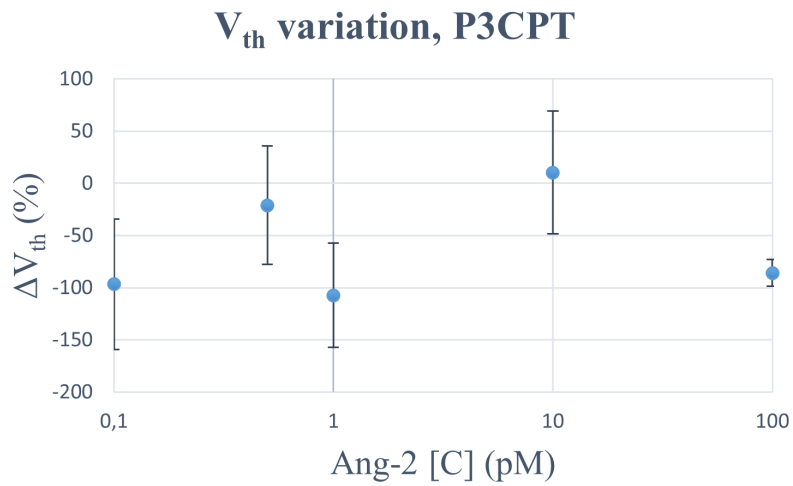


Figure 4.12: Variation of the maximum output current of a P3CPT-based EGO-FET during an Ang-2 sensing test. The increasing of the current is representative of the detection of binding events

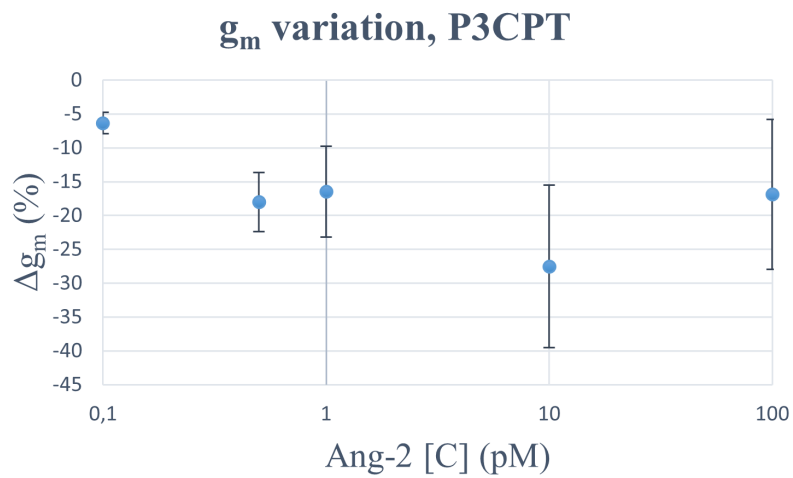
This is in contrast with the results discussed above since it overturns the charge dynamics: in this case, it seems that the additional layer of target molecules would make more difficult the carrier transport and consequently a higher voltage is needed to turn the device ON.

A possible explanation could be that some contamination between the analyte and the surface of the polymer is still present, so that a precise evaluation of the binding events is not possible. The exposed gate area could still be too high, thus providing a gate capacitance value not small enough to assure a sensitive and precise measurement.

Of course, process variations such as the manufacturing of the polymer leading to a non-homogeneous layer thickness or a non-uniform functionalization of the gate can add more unaccountable factors to the experiments that contribute to high variability of the results.

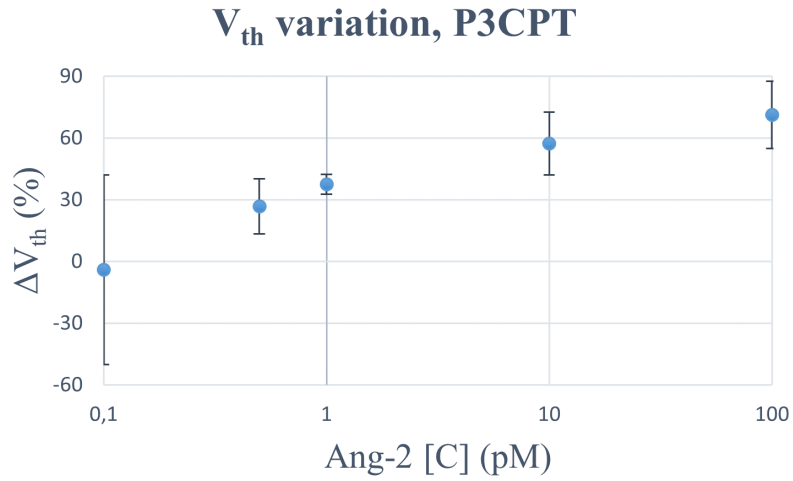


(a)

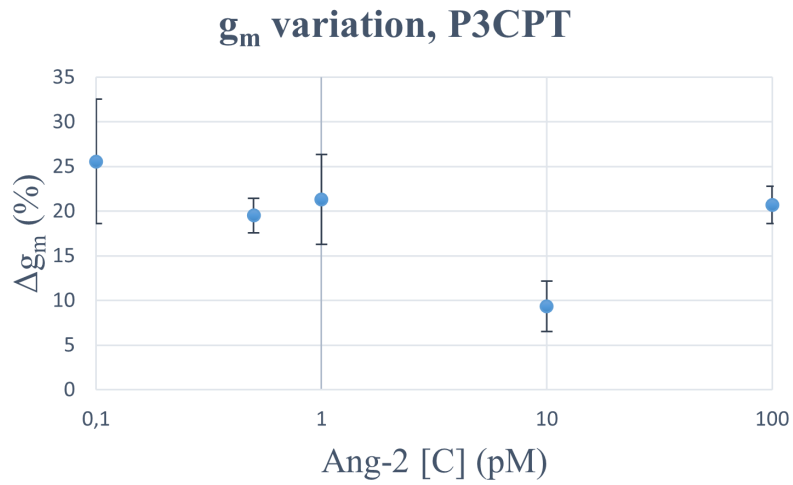


(b)

Figure 4.13: Variation of a) V_{th} and b) g_m of a P3CPT-based EGOFET during an Ang-2 sensing test. The detection of the binding events cannot be proven since it is not possible to recognize any particular trend



(a)



(b)

Figure 4.14: Variation of a) V_{th} and b) g_m of a P3CPT-based EGOFET during an Ang-2 sensing test. An opposite trend with respect to the expected one was recorded

Conclusions and future works

This work consists in the development and characterization of an EGOFET-based sensor for the detection of Angiopoietin-2 in physiological fluids.

A deep study of the effect of storage and electrical bias stress on the performances of the two used polymers, P3HT and P3CPT, was carried out, highlighting the main differences between the two and suggesting the physical mechanisms underneath the degradation in time.

From the obtained results, it seemed that storage in vacuum is to be avoided mostly for P3CPT, which turned out to be very stable when in contact with aqueous electrolyte. The reason could be an enhancement of polymer's performances due to electrochemical doping by water molecules that improves the carrier transport in the OSC, favoured by the higher hydrophilicity of P3CPT with respect to the P3HT.

Similarly, the electrical bias stress had a more deleterious effect on P3CPT rather than P3HT. The application of a prolonged bias had two opposite effects on the two polymers: it resulted in a reduced threshold voltage for P3HT that eventually stabilizes, which denotes an improvement of the carrier transport, while a continuous increase of V_{th} was recorded for P3CPT, which denotes a progressive degradation of the electrical properties of the polymer.

The different behaviors were ascribed to different physical mechanisms.

P3HT is able to establish a reversible charge-transfer complex with oxygen, which can improve the generation of carriers under the application of an electric field and eventually lead to an improvement of the transport. Moreover a complete recovery of both threshold voltages and transconductance is observable.

P3CPT seems to suffer the electrical bias stress because of some charge trapping phenomena involving bulk trap states, that prevent the transport of carriers and lead to the increase of the threshold voltage.

Of course, a deeper study is necessary in order to fully understand the physical origin

of the charge trapping mechanism, since a precise identification is still missing in literature.

Concerning the Ang-2 biosensing application, tests on P3CPT-based EGOFETs only were performed, since preliminary trials involving BSA highlighted the poor sensing performances of P3HT in the developed configuration, probably due to its low capacitance with respect to the gold gate one.

P3CPT-based devices provided many promising results and resulted to be quite sensitive to the presence of different concentrations of Ang-2, which adds negative charges to the systems and enlarges the output current.

Some criticalities were also recorded, denoting the poor replicability of the results. The reasons could be either contamination of the polymer by the target, either more technical issues such as the manufacturing of the polymer itself and of the functionalization layer on the gold surface.

Future works could improve the fabrication and manufacturing processes and explore different configurations of the device in order to find the best conditions that guarantee sensitivity, precision and stability of the device.

Bibliography

1. Park, J. *et al.* *Serum angiopoietin-2 as a clinical marker for lung cancer* 2007. <https://doi.org/10.1378/chest.06-2915>.
2. Takanami, I. *Overexpression of Ang-2 mRNA in non-small cell lung cancer: Association with angiogenesis and poor prognosis* 2004. <https://doi.org/10.3892/or.12.4.849>.
3. Zhizhen, D. *et al.* *Ang-2 promotes lung cancer metastasis by increasing epithelial-mesenchymal transition* 2018. <https://doi.org/10.18632/oncotarget.24061>.
4. Torsi, L., Magliulo, M., Manoli, K. & Palazzo, G. *Organic field-effect transistor sensors: A tutorial review* 2013. [10.1039/c3cs60127g](https://doi.org/10.1039/c3cs60127g).
5. Wang, Y., Zhang, J., Zhang, S. & Huang, J. *OFET chemical sensors: Chemical sensors based on ultrathin organic field-effect transistors*. 2021. <https://doi.org/10.1002/pi.6095>.
6. Wang, N., Yang, A., Fu, Y., Li, Y. & Yan, F. *Functionalized Organic Thin Film Transistors for Biosensing* 2019. <https://doi.org/10.1021/acs.accounts.8b00448>.
7. Kergoat, L. *et al.* *A water-gate organic field-effect transistor* 2010. [10.1002/adma.200904163](https://doi.org/10.1002/adma.200904163).
8. Wang, D., Noël, V. & Piro, B. *Electrolytic gated organic field-effect transistors for application in biosensors—A review* 2016. <https://doi.org/10.3390/electronics5010009>.
9. Berto, M., Diacci, C., D'Agata, R. & *et al.* *EGOFET Peptide Aptasensor for Label-Free Detection of Inflammatory Cytokines in Complex Fluids* 2018. <https://doi.org/10.1002/adbi.201700072>.
10. Sensi, M., Berto, M., Gentile, S. & *et al.* *Anti-drug antibody detection with label-free electrolyte-gated organic field-effect transistors* 2021. <https://doi.org/10.1039/d0cc03399e>.

11. Buth, F., Donner, A., Sachsenhauser, M., Stutzmann, M. & et al. *Biofunctional electrolyte-gated organic field-effect transistors* 2012. <https://doi.org/10.1002/adma.201201841>.
12. Casalini, S., Leonardi, F. & et al. *Organic field-effect transistor for label-free dopamine sensing* 2013. <https://doi.org/10.1016/j.orgel.2012.10.027>.
13. Tu, D., Forchheimer, R., Herlogsson, L., Crispin, X. & Berggren, M. *Parameter extraction for electrolyte-gated organic field effect transistor modeling* 2011. 10.1109/ECCTD.2011.6043825.
14. Tividis, Y. & McAndrew, C. *Operation and modeling of the mos transistor* ISBN: 9780195170153 (McGraw-Hill, 1999, 2011).
15. Du, H., Lin, X., Xu, Z. & Chu, D. *Electric double-layer transistors: a review of recent progress* 2015. 10.1007/s10853-015-9121-y.
16. Sedra, A. & Smith, K. *Microelectronic circuits, seventh edition* ISBN: 978-0-19-933913-6 (Oxford University Press, 2015).
17. Kergoat, L., Piro, B., Berggren, M., Horowitz, G. & Pham, M. C. *Advances in organic transistor-based biosensors: From organic electrochemical transistors to electrolyte-gated organic field-effect transistors* 2012. <https://doi.org/10.1007/s00216-011-5363-y>.
18. Picca, R. A. *et al. Ultimately Sensitive Organic Bioelectronic Transistor Sensors by Materials and Device Structure Design* 2020. <https://doi.org/10.1002/adfm.201904513>.
19. Tu, D. *et al. A static model for electrolyte-gated organic field-effect transistors* 2011. 10.1109/TED.2011.2162648.
20. Zhang, L. & Zhao, X. S. *Carbon-based materials as supercapacitor electrodes* 2009. <https://doi.org/10.1039/b813846j>.
21. Kim, S. H. *et al. Electrolyte-gated transistors for organic and printed electronics* 2013. <https://doi.org/10.1002/adma.201202790>.
22. Stern, E. *et al. Importance of the debye screening length on nanowire field effect transistor sensors* 2007. <https://doi.org/10.1021/nl071792z>.
23. Palazzo, G. *et al. Detection beyond Debye's length with an electrolyte-gated organic field-effect transistor* 2015. 10.1002/adma.201403541.
24. Chu, C. H. *et al. Beyond the Debye length in high ionic strength solution: Direct protein detection with field-effect transistors (FETs) in human serum* 2017. <https://doi.org/10.1038/s41598-017-05426-6>.

25. Lin, S. P. *et al.* *A reversible surface functionalized nanowire transistor to study protein-protein interactions* 2009. <https://doi.org/10.1016/j.nantod.2009.04.005>.
26. Liu, N., Chen, R. & Wan, Q. *Recent advances in electric-double-layer transistors for bio-chemical sensing applications* 2019. <https://doi.org/10.3390/s19153425>.
27. Fabiano, S., Braun, S., Fahlman, M., Crispin, X. & Berggren, M. *Effect of gate electrode work-function on source charge injection in electrolyte-gated organic field-effect transistors* 2014. <https://doi.org/10.1002/adfm.201302070>.
28. Kergoat, L. *et al.* *Tuning the threshold voltage in electrolyte-gated organic field-effect transistors* 2012. <https://doi.org/10.1073/pnas.1120311109>.
29. *Next generation on display* 2003. [https://doi.org/10.1016/s1369-7021\(03\)00126-3](https://doi.org/10.1016/s1369-7021(03)00126-3).
30. Rjoub, A., Tarawneh, B. & Alghsoon, R. *Active matrix organic light emitting diode displays (AMOLED) new pixel design* 2019. <https://doi.org/10.1016/j.mee.2019.04.001>.
31. Gaj, M. P. *et al.* *Organic light-emitting diodes on shape memory polymer substrates for wearable electronics* 2015. <https://doi.org/10.1016/j.orgel.2015.06.029>.
32. Park, H. L. & Lee, T. W. *Organic and perovskite memristors for neuromorphic computing* 2021. <https://doi.org/10.1016/j.orgel.2021.106301>.
33. Coppedè, N. *et al.* *Ion selective textile organic electrochemical transistor for wearable sweat monitoring* 2020. <https://doi.org/10.1016/j.orgel.2019.105579>.
34. Scharber, M. C. & Sariciftci, N. S. *Efficiency of bulk-heterojunction organic solar cells* 2013. <https://doi.org/10.1016/j.progpolymsci.2013.05.001>.
35. Boix, P. P., Nonomura, K., Mathews, N. & Mhaisalkar, S. G. *Current progress and future perspectives for organic/inorganic perovskite solar cells* 2014. <https://doi.org/10.1016/j.mattod.2013.12.002>.
36. Lee, C. P., Li, C. T. & Ho, K. C. *Use of organic materials in dye-sensitized solar cells* 2017. <https://doi.org/10.1016/j.mattod.2017.01.012>.
37. Gritsenko, K. P. & Krasovsky, A. M. *Thin-film deposition of polymers by vacuum degradation* 2003. <https://doi.org/10.1021/cr010449q>.
38. Mavukkandy, M. O. *et al.* *Thin film deposition techniques for polymeric membranes—A review* 2020. <https://doi.org/10.1016/j.memsci.2020.118258>.
39. Myers, J. D. & Xue, J. *Organic semiconductors and their applications in photovoltaic devices* 2012. <https://doi.org/10.1080/15583724.2011.644368>.

40. Kohler, A. & Bassler, H. *Electronic Processes in Organic Semiconductors. An introduction* ISBN: 978-3-527-33292-2 (Wiley-VCH Verlag GmbH & Co. KGaA, Boschstr. 12, 69469 Weinheim, Germany, 2015).
41. Jain, S. C., Willander, M. & Kumar, V. *Conducting organic materials and devices* ISBN: 978-0-12-752190-9 (Academic Press, 2007).
42. Chen, F. C. *Organic semiconductors* 2018. <https://doi.org/10.1016/B978-0-12-803581-8.09538-2>.
43. *C₂H₄ hybridization* <https://www.chemistrylibrary.org/2019/07/c2h4-hybridization.html>.
44. *The Hybridization of C₂H₄ orbitals* https://www.clipartmax.com/middle/m2H7i8N4d3H7K9N4_the-hybridization-of-c2h4-orbitals-sp2-hybridization-c2h4/.
45. <https://www.clutchprep.com/organic-chemistry/homo-lumo>.
46. Miller, A. & Abrahams, E. *Impurity Conduction at Low Concentrations* 1960. doi:10.1103/physrev.120.745.
47. Sosorev, A. Y. *Simple charge transport model for efficient search of high-mobility organic semiconductor crystals* 2020. <https://doi.org/10.1016/j.matdes.2020.108730>.
48. Sirringhaus, H. *et al. Two-dimensional charge transport in self-organized, high-mobility conjugated polymers* 1999. doi:10.1038/44359.
49. Reynolds, J. R., Thompson, B. C. & Skotheim, T. A. *Conjugated Polymers. Properties, Processing, and Applications* ISBN: 978-1-138-06570-3 (CRC Press, Taylor & Francis Group, 2015).
50. Assadi, A., Svensson, C., Willander, M. & Inganäs, O. *Field-effect mobility of poly(3-hexylthiophene)* 1988. <https://doi.org/10.1063/1.100171>.
51. Parmeggiani, M. *et al. P3HT processing study for in-liquid EGOFET biosensors: Effects of the solvent and the surface* 2019. <https://doi.org/10.3390/s19204497>.
52. Toss, H. *et al. On the mode of operation in electrolyte-gated thin film transistors based on different substituted polythiophenes* 2014. <https://doi.org/10.1016/j.orgel.2014.06.017>.
53. Laiho, A., Herlogsson, L., Forchheimer, R., Crispin, X. & Berggren, M. *Controlling the dimensionality of charge transport in organic thin-film transistors* 2011. <https://doi.org/10.1073/pnas.1107063108>.

54. Bellani, S. *et al.* *Reversible P3HT/oxygen charge transfer complex identification in thin films exposed to direct contact with water* 2014. <https://doi.org/10.1021/jp4119309>.
55. Minamiki, T., Hashima, Y., Sasaki, Y. & Minami, T. *An electrolyte-gated polythiophene transistor for the detection of biogenic amines in water* 2018. <https://doi.org/10.1039/c8cc02462f>.
56. Ludwigs, S. *P3HT Revisited – from Molecular Scale to Solar Cell Devices* ISBN: 978-3-662-45144-1 (Springer Heidelberg New York Dordrecht London, 2014).
57. *Image Reversal Resists and Their Processing* https://www.microchemicals.com/technical_information/image_reversal_resists.pdf.
58. Das, R. & Chanda, A. *Fabrication and Properties of Spin-Coated Polymer Films* 2016. doi:10.1007/978-3-319-39715-3.
59. Bain, C. D. *et al.* *Formation of Monolayer Films by the Spontaneous Assembly of Organic Thiols from Solution onto Gold* 1989. <https://doi.org/10.1021/ja00183a049>.
60. Li, L., Wang, S., Xiao, Y. & Wang, Y. *Recent Advances in Immobilization Strategies for Biomolecules in Sensors Using Organic Field-Effect Transistors* 2020. <https://doi.org/10.1007/s12209-020-00234-y>.
61. Veisheh, M., Zareie, M. H. & Zhang, M. *Highly selective protein patterning on gold-silicon substrates for biosensor applications* 2002. <https://doi.org/10.1021/1a025529j>.
62. Silin, V., Weetall, H. & Vanderah, D. J. *SPR studies of the nonspecific adsorption kinetics of human IgG and BSA on gold surfaces modified by self-assembled monolayers (SAMs)* 1997. <https://doi.org/10.1006/jcis.1996.4586>.
63. Scientific, T. *Easy molecular bonding: crosslinking technology*
64. Chiadò, A. *et al.* *Optimization and characterization of a homogeneous carboxylic surface functionalization for silicon-based biosensing* 2016. <https://doi.org/10.1016/j.colsurfb.2016.03.048>.
65. Picca, R. A. *et al.* *A Study on the Stability of Water-Gated Organic Field-Effect Transistors Based on a Commercial p-Type Polymer* 2019. <https://doi.org/10.3389/fchem.2019.00667>.
66. Manoli, K. *et al.* *Pulsed voltage driven organic field-effect transistors for high stability transient current measurements* 2014. <https://doi.org/10.1016/j.orgel.2014.06.034>.

67. Chang, Y. C., Kuo, M. Y., Chen, C. P., Lu, H. F. & Chao, I. *On the air stability of n -channel organic field-effect transistors: A theoretical study of adiabatic electron affinities of organic semiconductors* 2010. <https://doi.org/10.1021/jp1025625>.
68. Jones, B. A. *et al.* *High-mobility air-stable n-type semiconductors with processing versatility: Dicyanoperylene-3,4:9,10-bis(dicarboximides)* 2004. <https://doi.org/10.1002/anie.200461324>.
69. Sirringhaus, H. *Device physics of solution-processed organic field-effect transistors* 2005. <https://doi.org/10.1002/adma.200501152>.
70. Lee, H. *et al.* *Charge Trapping in a Low-Crystalline High-Mobility Conjugated Polymer and Its Effects on the Operational Stability of Organic Field-Effect Transistors* 2021. <https://doi.org/10.1021/acscami.0c20965>.
71. Zilker, S. J., Detcheverry, C., Cantatore, E. & De Leeuw, D. M. *Bias stress in organic thin-film transistors and logic gates* 2001. <https://doi.org/10.1063/1.1394718>.
72. Sharma, A. *et al.* *Proton migration mechanism for operational instabilities in organic field-effect transistors* 2010. <https://doi.org/10.1103/PhysRevB.82.075322>.
73. Gomes, H. L. *et al.* *Bias-induced threshold voltages shifts in thin-film organic transistors* 2004. <https://doi.org/10.1063/1.1713035>.
74. Mathijssen, S. G. J. *et al.* *Dynamics of threshold voltage shifts in organic and amorphous silicon field-effect transistors* 2007. <https://doi.org/10.1002/adma.200602798>.
75. Sirringhaus, H. *Reliability of organic field-effect transistors* 2009. <https://doi.org/10.1002/adma.200901136>.
76. Pernstich, K. P., Oberhoff, D., Goldmann, C. & Batlogg, B. *Modeling the water related trap state created in pentacene transistors* 2006. <https://doi.org/10.1063/1.2396924>.
77. Abdou, M. S. A., Orfino, F. P., Son, Y. & Holdcroft, S. *Interaction of oxygen with conjugated polymers: Charge transfer complex formation with poly(3-alkylthiophenes)* 1997. <https://doi.org/10.1021/ja964229j>.
78. Bobbert, P. A., Sharma, A., Mathijssen, S. G. J., Kemerink, M. & De Leeuw, D. M. *Operational stability of organic field-effect transistors* 2012. <https://doi.org/10.1002/adma.201104580>.
79. Minami, T., Tang, W. & Asano, K. *Chemical sensing based on water-gated polythiophene thin-film transistors* 2021. <https://doi.org/10.1038/s41428-021-00537-4>.

80. Guckeisen, T., Hosseinpour, S. & Peukert, W. *Isoelectric Points of Proteins at the Air/Liquid Interface and in Solution* 2019. <https://doi.org/10.1021/acs.langmuir.9b00311>.
81. Cho, M. *et al. Quantitative selection and parallel characterization of aptamers* 2013. <https://doi.org/10.1073/pnas.1315866110>.